Computational and Experimental Study of Li-Doped Ionic Liquids at Electrified Interfaces

Justin B. Haskins[†] and John W. Lawson[*,‡]

AMA Inc., Thermal Materials Protection Branch, Mail Stop 234-1, NASA Ames Research Center, Moffett Field, California 94035, USA, and Thermal Materials Protection Branch, Mail Stop 234-1, NASA Ames Research Center, Moffett Field, California 94035, USA

E-mail: john.w.lawson@nasa.gov

---

[*] To whom correspondence should be addressed

[†] AMA Inc., Thermal Materials Protection Branch, Mail Stop 234-1, NASA Ames Research Center, Moffett Field, California 94035, USA

[‡] Thermal Materials Protection Branch, Mail Stop 234-1, NASA Ames Research Center, Moffett Field, California 94035, USA

Abstract

We evaluate the influence of Li-salt doping on the dynamics, capacitance, and structure of three ionic liquid electrolytes, [pyr14][TFSI], [pyr13][FSI], and [EMIM][BF$_4$], using molecular dynamics and polarizable force fields. In this respect, our focus is on the properties of the electric double layer (EDL) formed by the electrolytes at the electrode surface as a function of surface potential (Ψ). The rates of EDL formation are found to be on the order of hundreds of picoseconds and only slightly influenced by the addition of Li-salt. The EDLs of three electrolytes are shown to have different energy storage capacities, which we relate to the EDL formation free energy. The differential capacitance obtained from our computations exhibits asymmetry about the potential of zero charge and is consistent with the camel-like profiles noted from mean field theories and experiments on metallic electrodes. The introduction of Li-salt reduces the noted asymmetry in the differential capacitance profile. Complementary experimental capacitance measurements have been made on our three electrolytes in their neat forms and with Li-salt. The measurements, performed on glassy carbon electrodes, produce U-like profiles, and Li-salt doping is shown to strongly affect capacitance at high magnitudes of Ψ. Differences in the theoretical and experimental shapes and magnitudes of capacitance are rationalized in terms of the electrode surface and pseudocapacitive effects. In both neat and Li-doped liquids, the details of the computational capacitance profile are well described by Ψ-induced changes in the density and molecular orientation of ions in the molecular layer closest to the electrode. Our results suggest that the addition of Li$^+$ induces disorder in the EDL, which originates from the strong binding of anions to Li$^+$. An in-depth analysis of the distribution of Li$^+$ in the EDL reveals that it does not readily enter the molecular layer at the electrode surface, preferring instead to be localized farther away from the surface in the second molecular layer. This behavior is validated through an analysis of the free energy of Li$^+$ solvation as a function of distance from the electrode. Free energy wells are found to coincide with localized concentrations of Li$^+$, the depths of which increase with Ψ and suggest a source of impedance for Li$^+$ to reach the electrode.

Keywords. molecular dynamics, differential capacitance, electric double layer, supercapacitor

Introduction

Recent material advances[1–3] have led to improvements in the energy density and delivery of electrochemical capacitors.[4] Typically, these utilize a liquid electrolyte to store energy non-Faradaically at the electrode surface, with the electrolyte interfacial layer being referred to as the electric double layer (EDL). As it stands, ionic liquids are appealing electrolytes[5–10] as they are more electrochemically stable than conventional organic electrolytes, which allows the use of a large voltage bias for greater energy storage. Furthermore, ionic liquids readily solvate Li^+ and have shown stable operation in Li-ion[11,12] and more advanced[13–17] batteries, which invites the possibility of developing hybrid battery/capacitor devices.[18] Combined with the favorable properties of ionic liquid electrolytes, nanostructuring the electrode interface to obtain high surface area and pores[19–29] can lead to further gains in capacitance, though more exact optimization in this way will require an in-depth understanding of the interplay between electrode and EDL structure.

An important measure of the ability of a given electrolyte to store energy at an electrode is the differential capacitance (C_{dl}), which is defined as the rate of change of surface charge density ($\langle\sigma\rangle$) with surface potential ($\langle\Psi\rangle$), or $\partial\langle\sigma\rangle/\partial\langle\Psi\rangle$. C_{dl} is a highly sensitive function of electrolyte molecular size, weight, and shape and can thus provide information regarding the structure of the EDL. In this respect, the tolerance of C_{dl} to electrolyte molecule characteristics has been extensively investigated, particularly the dependence of chain length of various imidizolium and pyrrolidinium cations, the size of fluorinated anions (*e.g.* $[BF_4]^-$ versus $[PF_6]^-$), and the weight of elemental halogen anions.[5,7–10,30–32] Broadly speaking, the results show that C_{dl} assumes characteristic profiles in different liquids, which include the single maximum "bell," the dual maxima "camel," and single minimum "U" profiles,[31] while the magnitudes are generally[3] between 5-20 $\mu F/cm^2$. Furthermore, the potential of zero charge ($\langle\Psi\rangle^0$) determined from these profiles is generally assumed to be at an extrema, either the peak of the bell curve or the valley of the camel curve. C_{dl} often exhibits anisotropy about this point, which can be exacerbated by large disparities in cation and anion size.

As a means of obtaining a more detailed understanding of the interplay between EDL structure and capacitance, several experimental approaches have been developed to quantify molecular density and configuration at the electrode surface under potential bias. Both X-ray reflectivity[33–36] and atomic force microscopy[37–42] yield general information on ion distribution within the EDL. These methods have been used to characterize the layered structure (*i.e.* alternating layers of cations and anions) of the EDL and, in specific cases, have provided coarse information about surface ion configuration.[39] Other methods, including X-ray photoelectron spectroscopy[43] and sum frequency generation spectroscopy[44–48] allow the resolution of finer details of surface ions, including average orientations of ion moieties with respect to the surface.

With respect to theory, the mean field theory lattice gas model developed by Kornyshev[49] correlates ion structure to differential capacitance. The mean field approach expands upon the earlier Guoy-Chapman-Stern model of the response of dilute electrolytes to electrified interfaces to include the effect of ion size and density, which are important in dense ionic systems. Through the incorporation of these effects, the mean field model successfully reproduces the characteristic "bell" and "camel" $\mathrm{C_{dl}}$ profiles noted in experiment,[3,49–52] with differences between the packing efficiency of anions and cations at the electrode surface leading to the aforementioned anisotropy about $\langle\Psi\rangle^0$. However, because detailed molecular correlation effects are difficult to include in the mean field model, the resulting $\mathrm{C_{dl}}$ captures only the most general aspects of differential capacitance, though more complex theories that incorporate ion correlation effects have been proposed.[53]

Alternatively, molecular dynamics (MD) simulations can provide atomic-level insight into the behavior of ionic liquids at electrified interfaces. Such simulations have show success in detailing the structure of the EDL,[54–56] the EDL capacitance as a function of $\langle\Psi\rangle$,[25,57–65] and the influence of electrode structure (e.g. porosity and curvature) on EDL behavior.[20,23,24,26–28,66–74] Of note, recent united atom MD simulations have been used to explore the structural origin of C_{dl} for a number of ionic liquids.[24,29,61,62,74,74,75] These simulations have successfully correlated C_{dl} to the structure of ions at the surface of both ideal[24,29,61,62,74,75] and non-ideal electrodes.[74]

The present work extends the use of MD simulations to the study of Li-doped ionic liquids at electrified interfaces. In general, there have been few investigations on this topic, despite its importance for batteries and hybrid battery/capacitor devices.[76,77] This is related perhaps to the complex energetics of Li^+ solvated in ionic liquids, which can be difficult to represent with conventional force fields.[78,79] These issues are overcome here by using the atomic polarizable potential for liquids, electrolytes, and polymers (APPLE&P),[80–82] which accurately captures the energetics and dynamics of a range of Li-doped ionic liquids.[78,79,83,84] Furthermore, the use of APPLE&P allows the electrolyte to polarize in response to an electrified interface, which has been shown to impact both the EDL structure and capacitance.[85] We perform these simulations on three ionic liquids of electrochemical interest,[11–17] *N*-methyl-*N*-butylpyrrolidinium bis(trifluoromethanesulfonyl)imide ([pyr14][TFSI]), *N*-methyl-*N*-propylpyrrolidinium bis(fluorosulfonyl)imide ([pyr13][FSI]), and 1-ethyl-3-methylimidazolium boron tetrafluoride ([EMIM][BF_4]), in both their neat and Li-doped form. The simulations are performed using a model capacitor system with two electrodes (see Fig. 1) having a constant potential difference ($\Delta\Psi$) imposed by dynamically updating surface charge throughout the simulation. We investigate these liquids for $0\ \mathrm{V} \leq \Delta\Psi \leq 4.2\ \mathrm{V}$, which is approximately within the electrochemical windows of the electrolytes, and for Li-salt mole fractions (x_{Li}) of 0.0 and 0.2.

As an outline of this work, we first evaluate the influence of Li^+ on the most general aspects of the EDL evolved at the electrode surface, including formation times, energetic content, and differential capacitance, where differential capacitance is computed with a modified version of recently developed fluctuation formulas.[56,85] The properties are then correlated to the molecular structure of the EDL by analyzing the ion density and configuration at the interface. Finally, we complement the structural analysis by a detailed examination of the distribution, binding and solvation free energy of Li^+ in the EDL.

Methods

Ionic Liquid Interatomic Potential

We employ the atomic polarizable potential for liquids, electrolytes, and polymers (APPLE&P) as parameterized by Borodin and coworkers[80–82] for the ionic liquids of interest in the present work. Through extensive testing,[79,81,83,84,86] APPLE&P has been shown to accurately capture the thermodynamic behavior of a vast array of ionic liquids as well as ionic liquid systems containing Li-salt. While many of the energetic interactions in APPLE&P are standard to molecular dynamics simulations, including harmonic bonded interactions, the exponential-6 Buckingham potential, and Coulomb interactions between point charges, APPLE&P includes a self-consistent measure of atomic polarization. Each atom is assigned an atomic polarizability (α) which yields an atomic dipole moment ($\boldsymbol{\mu}$) proportional to the electric field, $\boldsymbol{\mu}_i = \alpha \mathbf{E}(\mathbf{r}_i)$. To obtain the induced dipoles, one must iteratively update the electric field with induced dipole contributions until the total polarization energy,

$$U^{pol} = -\frac{1}{2}\sum_i \boldsymbol{\mu}_i \cdot \mathbf{E}^0(\mathbf{r}_i), \tag{1}$$

where $\mathbf{E}^0(\mathbf{r}_i)$ is the electrostatic field contribution from permanent charges only, converges. Further details of the force field as used for these ionic liquids can be found elsewhere.[79–81]

Electrode Model

The model capacitor employed here is composed of two electrodes, between which is ionic liquid, as shown in Fig. 1. The use of two electrodes is a practical means of creating electrified interfaces while maintaining charge neutrality (*i.e* each system is composed of a negative and positive electrode that are oppositely charged). The geometry of our model capacitor is taken to be that of a slab, with the system being periodic in the (x,y), or in-plane, directions and having a finite thickness L_{z} in the z-direction. The region beyond the electrodes in the z-direction is assumed to be an infinite vacuum. Problematically, standard long range electrostatic summation techniques, namely the Ewald summation and particle-mesh methods, assume the system has full three dimensional periodicity, which is not appropriate for slab geometries employed here. To correct for this, there are exact forms of the two dimensional Ewald summation[87] as well as corrections to the three dimensional Ewald summation that approximate slab conditions.[88] As described in detail elsewhere,[85] we have tested both approaches in slab systems and have found the correction to the three dimensional Ewald to be in excellent agreement with the two dimensional Ewald summation. The correction method, as originally described by Yeh and coworkers,[88] assumes a system of slab geometry being separated by a suitable distance from its periodic image normal to the slab such that mutual slab-slab interactions are approximately dipolar. Though originally developed for systems of interacting point charges, we have extended this correction to account for the long-range interaction of point charges with the atomic dipoles produced from the polarizable force field, yielding

$$U_{corr}^{2D} = \frac{1}{2\epsilon_0} M_z^2, \tag{2}$$

where ϵ_0 is the permittivity of free space and M_z is the net dipole moment in the z-direction, $\sum_{i=1}^{N} (q_i z_i + \mu_{zi})$.

The electrodes are treated as rigid bodies, with the positions of the electrode atoms held fixed throughout the simulations. The electrode atoms interact with the ionic liquids through both repulsive dispersive interactions, as described by the Buckingham potential, as well as through electrostatic interactions. To approximate the electrode surface as metallic, we follow the convention[89] of treating charges on electrode atoms as Gaussians with a half maximum width of 0.5; the electrode atoms do not have induced dipoles. A constant potential difference ($\Delta\Psi$) is maintained between the electrodes during a given simulation. This is achieved by dynamically distributing electrode charge using a modified version of a procedure first implemented by Siepmann[89] and later adapted to interactions between electrified interfaces and organic and ionic liquid electrolytes.[61,63,90] In this approach the total Hamiltonian, H, is given by

$$H = U^K + U^{RD} + U^{ES} - A|\sigma|\Delta\Psi, \tag{3}$$

where U^K is kinetic energy, U^{RD} is the repulsive-dispersive energy, U^{ES} is the total electrostatic energy, A is the electrode surface area, $|\sigma|$ is the absolute value of the electrode surface charge density on either the positive (σ^+) or negative (σ^-) electrode ($\sigma^+ = -\sigma^-$), and $\Delta\Psi = \Psi^+ - \Psi^-$ is the potential difference set between the positive (Ψ^+) and negative (Ψ^-) electrodes. As detailed elsewhere,[85] the charges on the electrode atoms are updated under the constraint that the charge on the positive electrode balances that on the negative electrode until $\partial H/\partial q_i^+ = \partial H/\partial q_i^- = 0$, where q_i^+ and q_i^- are charges on individual atoms in the positive or negative electrode.

EDL Thermodynamics

We now derive several useful thermodynamic relationships for the EDL free energy and capacitance that can be evaluated from MD simulations that employ our model capacitor with the constant-$\Delta\Psi$ condition. The Helmholtz free energy of our model capacitor, F, can be written as, $\mathrm{F} = -\beta^{-1}\ln(\Omega)$, where β is defined as the inverse product of Boltzmann's constant and temperature ($1/k_bT$), H is the Hamiltonian of our system defined in Eq. 3, and Ω is the partition function of the system, which is given by the integral of $e^{-\beta H}$ over phase space. The partial derivative of F with respect to $\Delta\Psi$ is then given by,

$$\frac{\partial F}{\partial \Delta\Psi} = -A\langle|\sigma|\rangle - A\Delta\Psi\left\langle\frac{\partial|\sigma|}{\partial\Delta\Psi}\right\rangle + \left\langle\frac{\partial U^{ES}}{\partial\Delta\Psi}\right\rangle, \tag{4}$$

where the terms containing $\langle\partial|\sigma|/\partial\Delta\Psi\rangle$ and $\langle\partial U^{ES}/\partial\Delta\Psi\rangle$ arise from implicit, instantaneous dependencies of charge and energy on $\Delta\Psi$ introduced by the constant-$\Delta\Psi$ procedure. By integrating this function over $\Delta\Psi$, one may obtain the free energy of EDL formation on both electrodes.

It is more informative, however, to obtain changes in F for the charging of individual electrode surfaces (*i.e.* separating the energetic contributions of the positive and negative electrodes), or $\partial F/\partial\langle\Psi\rangle$. Such a value can be expanded as

$$\frac{\partial F}{\partial\langle\Psi\rangle} = \frac{\partial F}{\partial\Delta\Psi}\frac{\partial\Delta\Psi}{\partial\langle\Psi\rangle}. \tag{5}$$

Taking the derivative of the ensemble average of surface potential difference, given by $\langle\Psi\rangle = \int \Psi e^{-\beta H}dr/\int e^{-\beta H}dr$, where β is the inverse product of temperature with Boltzmann's constant and r represents the atomic configuration of our system, with respect to $\Delta\Psi$ leads to

$$\left[\frac{\partial\Delta\Psi}{\partial\langle\Psi\rangle}\right]^{-1} = \left\langle\frac{\partial\Psi}{\partial\Delta\Psi}\right\rangle + \beta A\left\langle|\sigma|\delta\Psi\right\rangle. \tag{6}$$

For the systems of interest in the present work, we have found numerically that $\langle\partial\Psi/\partial\Delta\Psi\rangle$, representing the instantaneous change of electrode potential with a change in potential difference, is approximately ±0.5, while the fluctuation of potential, $\delta\Psi = \Psi - \langle\Psi\rangle$, and surface charge can be easily obtained during the molecular dynamics simulation. Combining Eq. 5 and Eq. 6, one obtains

$$\Delta F^{\text{edl}} = \int_{\langle\Psi\rangle^0}^{\langle\Psi\rangle^f}\frac{\partial F}{\partial\Delta\Psi}\left[\left\langle\frac{\partial\Psi}{\partial\Delta\Psi}\right\rangle + \beta A\langle|\sigma|\delta\Psi\rangle\right]^{-1} d\langle\Psi\rangle, \tag{7}$$

where ΔF^{edl} is the potential dependent EDL formation free energy difference between the potential of zero charge, $\langle\Psi\rangle^0$ and $\langle\Psi\rangle^f$.

As detailed elsewhere,[56,85] fluctuation formulas can be derived to define $\mathrm{C_{dl}}$ as a function of $\langle\Psi\rangle$. As with free energy before, one may take the derivative of the average surface charge, $\langle\sigma\rangle = \int \sigma e^{-\beta H} dr / \int e^{-\beta H} dr$, with respect to $\Delta\Psi$ to approximately yield

$$\frac{\partial\langle\sigma\rangle}{\partial\Delta\Psi} = \left\langle \frac{\partial\sigma}{\partial\Delta\Psi} \right\rangle + \beta A \left\langle |\sigma| \delta\sigma \right\rangle , \tag{8}$$

where $\langle\partial\sigma/\partial\Delta\Psi\rangle$ is again attributed to implicit dependencies of charge on the defined value of $\Delta\Psi$.

This represents the total differential capacitance of our two-electrode, model capacitor. The capacitance of an isolated electrode is valuable for understanding the comparative behavior of EDLs at the positive and negative electrodes. To obtain such a quantity, we can write $\partial\langle\sigma\rangle/\partial\langle\Psi\rangle = \partial\langle\sigma\rangle/\partial\Delta\Psi \times \partial\Delta\Psi/\partial\langle\Psi\rangle$, which, when combined with Eq. 6, gives

$$\frac{\partial\langle\sigma\rangle}{\partial\langle\Psi\rangle} = \frac{\partial\langle\sigma\rangle}{\partial\Delta\Psi} \left[\left\langle \frac{\partial\Psi}{\partial\Delta\Psi} \right\rangle + \beta A \left\langle |\sigma| \delta\Psi \right\rangle \right]^{-1} . \tag{9}$$

The complete derivation of this equation is described elsewhere.[85]

As a final note on the thermodynamic expressions, one may leverage Eq. 8 to rewrite ΔF^{edl} in terms of surface charge. Starting with $\partial F/\partial\langle\sigma\rangle = \partial F/\partial\Delta\Psi \times \partial\Delta\Psi/\partial\langle\sigma\rangle$, the charge dependent free energy of EDL formation is given as

$$\Delta F^{\mathrm{edl}} = \int_0^{\langle\sigma\rangle^f} \frac{\partial F}{\partial\Delta\Psi} \left[\left\langle \frac{\partial\sigma}{\partial\Delta\Psi} \right\rangle + \beta A \left\langle |\sigma| \delta\sigma \right\rangle \right]^{-1} d\langle\sigma\rangle, \tag{10}$$

where ΔF^{edl} is the free energy difference between the system having, on average, no electrode charge to a value of $\langle\sigma\rangle^f$.

Solvation Free Energy

To understand the interplay between surface structure and Li-salt doping, we perform a free energy analysis on Li^+ solvation in the EDL as a function of Δz and $\langle \Psi \rangle$. In general, the solvation free energy of a given molecule is computed along a thermodynamic cycle that takes the molecule from a gaseous state to a solvated state in a liquid bath. However, the solvation of a single ion, like Li^+, into an electrolyte leads to a charge imbalance, which can lead to errors that makes the determination of solvation free energy difficult. To overcome this difficulty, we compute the free energy using a thermodynamic cycle that solvates Li^+ into the electrolyte of our model capacitor system and simultaneously balances the resulting charge by countercharging an electrode. The simplest form of such a cycle is

$$F^s(0) = \Delta F^{\mathrm{Li}^0(g) \rightarrow \mathrm{Li}^0(l)} + \Delta F^{\mathrm{Li}^0(l) \rightarrow \mathrm{Li}^+(l)}_{\sigma=0 \rightarrow \sigma=-1} - \Delta F^{\mathrm{edl}}. \tag{11}$$

We first compute the solvation free energy of a neutral Li^0 from a gaseous state to a solvated state in the electrolyte of our model capacitor system, given by $\Delta F^{\mathrm{Li}^0(g) \rightarrow \mathrm{Li}^0(l)}$. This interaction is mediated through repulsive-dispersive interactions and the response of Li^+ polarizability to the electrolyte. To ensure the Li^0 is solvated into the bulk-like region, we constrain the trajectory of Li^+ over the course of the MD simulation to ensure the value of z is zero, or at the midpoint between our electrodes (such a procedure is later validated by our results, which show a constant value of solvation free energy when $\Delta z > 20$ Å from the electrode surface). We then calculate the free energy of charging Li^0 to Li^+ while simultaneously balancing the ion by charging one of the electrodes to a value of -1 a.u., $\Delta F^{\mathrm{Li}^0(l) \rightarrow \mathrm{Li}^+(l)}_{\sigma=0 \rightarrow \sigma=-1}$, which overcomes the charge imbalance issues encountered when solvating an ion into a bulk liquid system. The solvation free energy of Li^+ at $z = 0$, $\Delta F^s(0)$, can then be obtained by removing ΔF^{edl} induced from charging the electrode through Eq. 10. We later denote $\Delta F^{\mathrm{Li}^0(l) \rightarrow \mathrm{Li}^+(l)}_{\sigma=0 \rightarrow \sigma=-1} - \Delta F^{\mathrm{edl}}$ as simply $\Delta F^{\mathrm{Li}^0(l) \rightarrow \mathrm{Li}^+(l)}$, or the free energy of charging the Li^+.

To understand barriers to Li^+ translation within the EDL, we perform additional computations to determine the change in free energy as a function of z, or distance from the electrode, Δz. We first perform MD simulations having Li^+ constrained to various values of z throughout the EDL and, for each simulation, determine the average value of force on Li^+ in the z-direction, $\langle f_z^{\mathrm{Li}} \rangle$. The formalism known as the "blue-moon" ensemble[91] relates the constrained forces to the derivative in free energy with respect to z-direction translation. This results in our z-dependent solvation free energy taking the form

$$F^s(z) = F^s(0) - \int_0^z \langle f_z^{\mathrm{Li}^+} \rangle|_{z'} dz', \tag{12}$$

where $\langle f_z^{\mathrm{Li}^+} \rangle|_{z'}$ represents the z-directional force when Li^+ is constrained to z'. Similar approaches without constraints have been employed successfully to study ion free energetics within the EDL.[77,92–94] However, our use of a constraint-based method allows a better probe of regions where Li^+ density is negligible over the course of a standard MD simulation, which can lead to more accurate averaging of $\langle f_z^{\mathrm{Li}} \rangle|_{z'}$

Molecular Dynamics Simulations

We have performed MD simulations on six ionic liquid systems in total, which include [pyr14][TFSI], [pyr13][FSI], and [EMIM][BF_4] having x_{Li} values of 0.0 and 0.2. Our simulations employ three-layer graphite electrodes interfaced with the ionic liquids; the normal of the basal plane defines the z-direction. The distance between the electrode surfaces is 10 nm, as shown in Fig. 1, which our tests have indicated results in practically non-interacting double layers; the in-plane, periodic dimensions are 2.46 nm × 2.58 nm. The systems are constructed by first equilibrating a large ionic liquid bath to the desired T and P conditions. Upon reaching equilibrium, the electrodes are inserted into the bath, and a stoichiometric number of ionic liquid pairs are removed to create a 3.14 Å vacuum buffer region around the electrodes. The system is then allowed to equilibrate under isobaric-isothermal conditions (NPT) for 10 ns, after which the average number of ion pairs in the electrode region can be obtained. We then generate electrode systems with slab geometry (periodic in the x and y directions only) filled with the number of ionic liquid pairs determined from the bath simulations. For reference, both the net system size and total simulation lengths are provided in Table 1.

The MD simulations in the present work are performed at $T = 363$ K, which is elevated when compare to most experiments on capacitors. This is necessary, however, to increase the glassy dynamics of Li-doped ionic liquids so that the EDL structure and capitative behavior can be suitably represented on MD time-scales. Time-integration is performed by the rRESPA[95] algorithm and a timestep of 3.0 fs, with the multiple time step partitions being provided in a previous work.[79] The long range electrostatics are performed with a coupled Ewald summation/reaction field formalism, whereby charge-charge and charge-dipole interactions are performed with an Ewald summation and dipole-dipole interactions are evaluated using a reaction field. The dipoles are updated self-consistently until the net dipole energy changes by less than 10^{-8} kcal/mol. Local non-bonded interactions, which include explicit Coulomb and repulsive-dispersive interactions, are performed within a cutoff of 12 Å for the [pyr14][TFSI] and the [pyr13][FSI] systems and 11 Å for the [EMIM][BF_4] systems. The electrode charge is updated every five time steps in the outermost rRESPA parition with the constant potential formalism such that the error in $\Delta\Psi$ is less than 0.05 V.

Experimental Techniques

The [pyr14][TFSI] (99%), [pyr13][FSI] (99.9%), and [EMIM][BF_4] were purchased from IOLITEC, Solvionic, and Fliua Analytical respectively. The corresponding salt, Li[TFSi] (>99.0%) and Li[BF_4] (99.998%) were purchased from Aldrich, and Li[FSI] (99%) was purchased from Sarchem Laboratories. All the ionic liquids and the corresponding salts were dried at 120^{o}C under vacuum for 10 hours before use. The differential capacitance measurements were completed in a Swagelok (USA) cell using glassy carbon (purchased from BAS) as working electrode, a coiled platinum (Pt) wire as a counter electrode, and a silver (Ag) wire as reference. The glassy carbon electrode was first polished following the procedures suggested from the vendor. All the cell components were dried at 90^oC under vacuum for 2 hours. The cell was then assembled and the ionic liquids were introduced in a the glove box. A Solartron 1287 potentiostat/galvanostat in combination with a model 1255B frequency response analyzer was used for cyclic voltammetry (CV) and electrochemical impedance spectroscopy (EIS) experiments (performed at room temperature). AC signal of 10 mV amplitude with frequency 1000 Hz at different DC voltage was used for the potential-dependent capacitance measurement. The measured impedance was normalized to the geometric electrode area.

Results

EDL Formation and Capacitance

Formation Times

The dynamics of EDL formation can be determined by considering the evolution of σ from a $\Delta\Psi = 0$ to a $\Delta\Psi > 0$ state as a function of time. We initially equilibrate our ionic liquid systems at 363 K and $\Delta\Psi = 0$ V for 10 ns. Using the system so equilibrated, we impose a non-zero $\Delta\Psi$ and track surface charge density until it converges, as shown in Fig. 2 for ionic liquids exposed to electrodes having $\Delta\Psi$ values of 2.1 and 4.2 V. For the potentials investigated, the surface charge reaches an equilibrium value in less that 1 nanosecond, though the exact value appears to be dependent on Li-salt content. We quantify the formation rate in Table 2 through a characteristic formation time, τ_{edl}, that is obtained from a simple fit of surface charge, given by $\sigma = \langle\sigma\rangle(1-e^{-t/\tau_{\mathrm{edl}}})$, where $\langle\sigma\rangle$ is the average value of surface charge density and t is time. A comparison of τ_{edl} across the ionic liquid systems shows that the formation time in [pyr14][TFSI] > [pyr13][FSI] > [EMIM][BF_4]. Interestingly, this hierarchy is inverse to that of the diffusion coefficient, implying liquids with higher diffusion coefficients exhibit faster EDL formation times and thereby faster charging. Furthermore, both surface potential and Li-salt doping have a strong effect on the charging times. The difference in the value of τ_{edl} at $\Delta\Psi = 2.1$ V versus 4.2 V changes from 193 ps to 318 ps, 64 ps to 216 ps, and 33 to 48 ps for [pyr14][TFSI], [pyr13][FSI], and [EMIM][BF$_4$], respectively. The effect of Li-salt doping is to increase τ_{edl} by a factor of ~2-5 with $\Delta\Psi = 2.1$ V and $\sim 1.2 - 3$ with $\Delta\Psi = 4.2$ V, which, sensibly, suggests the effect of Li$^+$ on EDL formation is reduced under a larger driving force, $\Delta\Psi$.

Differential Capacitance

The differential capacitance of our neat and Li-doped ionic liquid systems is shown in Figure 3. For all three liquids at $\Delta\Psi \leq 4.2$ V, we find that C$_{\mathrm{dl}}$ ranges from 3 to 6 μF/cm^2, depending on $\langle\Psi\rangle$. The average values of C$_{\mathrm{dl}}$ are markedly similar for our three liquids, 4.4, 4.5, and 4.5 μF/cm^2 for neat [pyr14][TFSI], [pyr13][FSI], and [EMIM][BF$_4$], respectively. At high values of $\langle\Psi\rangle$ we see, as expected, lower values of differential capacitance. These results agree well with previous MD simulations on ionic liquids,[24,61,62] which yield average values between 4-6 μF/cm^2. The agreement of our results with experiment, however, is less clear, with ionic liquids on various electrode materials and probed with various techniques yielding very different values of C$_{\mathrm{dl}}$. The general range of experimentally determined differential capacitance of ionic liquids spans 2-20 μF/cm^2,[5,7–10,96–98] which bounds our results. The probable explanation for higher experimental values and variances of C$_{\mathrm{dl}}$ are pseudo-capitative processes that include, namely, ion adsorption onto the electrode. Our MD simulations do not currently account for these effects but rather provide a pure measure of the EDL mediated capacitance.

Addressing the ionic liquids systems having $\mathrm{x_{Li}} = 0$, as shown in Figure 3 a,c, and e, we see that each system displays a distinct C$_{\mathrm{dl}}$ profile. For [pyr14][TFSI] and [pyr13][FSI], we note that $\mathrm{C_{dl}}$ assumes the characteristic "camel" shape, with [pyr14][TFSI] having a large peak occurring between 0 V and 1V and [pyr13][FSI] having a larger peak differential capacitance at negative potentials. Both of these features agree with previous united atom simulations of neat [pyr13][TFSI] and [pyr13][FSI] ionic liquids.[24,61,62] On the other hand, results for [EMIM][$\mathrm{BF_4}$] are only slightly asymmetric, with an incrementally higher maximum value of $\mathrm{C_{dl}}$ at negative potentials. For the systems having Li-salt, we see subtle differences in the shapes of $\mathrm{C_{dl}}$ in all three systems, while the average magnitudes of $\mathrm{C_{dl}}$ are not significantly different from those of the $\mathrm{x_{Li}} = 0$ systems. The primary impact of Li-doping on $\mathrm{C_{dl}}$ appears to be a softening of the asymmetry between positive and negative potentials, the origin of which will be probed later through a structural analysis. In all cases, we find that $\mathrm{C_{dl}}$ roughly has a minima at $\langle\Psi\rangle^0$, and this corresponds to the midpoint of the antisymmetric "camel" profile.

Experimental measurements, complimentary to our simulations, are shown in Figure 4 for the three ionic liquids of interest in the present work in both the neat form and having $\mathrm{x_{Li}} = 0.2$. For the neat systems, $\mathrm{C_{dl}}$ is U-like in character and has an average magnitude of 13.9, 27.2, and 9.9 $\mu\mathrm{C/cm^2}$ for [pyr14][TFSI], [pyr13][FSI], and [EMIM][$\mathrm{BF_4}$], respectively. Similarly, for the Li-doped systems, differential capacitance adopts the U-shaped profile and has an average magnitude of 16.0, 17.4, and 16.5 $\mu\mathrm{C/cm^2}$ for [pyr14][TFSI], [pyr13][FSI], and [EMIM][$\mathrm{BF_4}$], respectively. The addition of Li-salt appears to generally increase capacitance at higher surface potentials, likely due to plating or Li-mediated pseudo-capacitive processes. The major exception to this is found in [pyr13][FSI] system, which exhibits a reduction in capacitance upon addition of Li-salt.

Comparing our computational and experimental results is challenging as the systems are fundamentally different on a number of levels. First of all, the basic shape of capacitance is camel-like in our computational results and U-like in our experimental results. For a given ionic liquid, glassy carbon electrodes have been shown[31] to lead to more U-like $\mathrm{C_{dl}}$ profiles, while metallic electrodes produce capacitance profiles that are more camel-like. As we treat our model electrode as an ideal metal, the camel-like character is dominant and reasonable. Our computational differential capacitance also provides a lower bound to the experimental measurements. Surface roughness, such as that present on such glassy carbon surfaces, has been shown to lead to anomalous increases in capacitance.[29] Addressing the overall magnitude, our theoretical results an experiments are most similar at low values of surface potential, where one would expect the smallest influence from pseudocapacative effects (*e.g* adsorption and decomposition). At large magnitudes of surface potential, such processes certainly influence the value of capacitance. The surface structure of our ideal electrode is quite different from that of a glassy carbon electrode, and our computational models do not account for pseudo-capacitive processes.

Free Energy of Formation

Leveraging the fluctuations obtained from our differential capacitance computations, we apply Eq. 7 to obtain ΔF^{edl}, as shown in Figure 5, which, along with $\langle \sigma \rangle$, is displayed as a function of $\langle \Psi \rangle$ for our electrolytes in their neat form. Each of the ΔF^{edl} profiles exhibits a quasi-parabolic behavior as a function of $\langle \Psi \rangle$ and are predominantly symmetric. The fact that the asymmetry in $\mathrm{C_{dl}}$ does not strongly manifest in these systems in not entirely surprising as, at a given value of $\Delta\Psi$, the difference in $\mathrm{C_{dl}}$ between the two electrodes is generally < 1 μF/cm^2. The relative ordering of ΔF^{edl} between the three liquids appears to change depending on the $\langle \Psi \rangle$ range. At $\langle \Psi \rangle < 0.0$ V, the value of ΔF^{edl} in [EMIM][BF$_4$] $<$ [pyr14][TFSI] $<$ [pyr13][FSI] until $\langle \Psi \rangle \leq -1.5$ V, where [pyr13][FSI] rapidly overtakes the other liquids to have the smallest value of ΔF^{edl} at $\langle \Psi \rangle \sim -2.1$ V. At $\langle \Psi \rangle > 0.0$ V, we see similar values of ΔF^{edl} between the systems, though [EMIM][BF$_4$] is slightly higher, until $\langle \Psi \rangle \sim 1$ V, where with increasing potential ΔF^{edl} in [pyr13][FSI] $<$ [EMIM][BF$_4$] $<$ [pyr14][TFSI]. Of course, a liquid having a smaller value ΔF^{edl} is generally implied from larger values of $\langle \sigma \rangle$ across a potential range, which follows from Eq. 4. To this point, at the extreme values of $\langle\Psi\rangle$, $\sim \pm 2.1\ V$, $|\langle|\sigma|\rangle|$ is found to be 9.11, 9.99, and 9.52 μC/cm^2 for [pyr14][TFSI], [pyr13][FSI], and [EMIM][BF$_4$], respectively, which reflects the aforementioned the order of ΔF^{edl} at these potentials. In the case of liquids having Li-salt, we note that there are only slight changes in the free energetics, with the energies of the three liquids again having magnitudes and orderings similar to those of the neat system.

EDL Structure

Ion Density Profiles

As an initial means of characterizing the influence of Li-doping on the structure of the EDL, we now look at average ion density profiles as a function of distance from the electrode, $\rho(\Delta\mathrm{z})$. In this way, $\rho(\Delta\mathrm{z})$ is computed on a per atom basis and normalized by the total number of ion atoms in the simulation cell. Though we have performed computations with various values of $\Delta\Psi$, we choose representative values that give an adequate sampling of the structures observed in our simulations, namely the equipotential condition, $\Delta\Psi = 0$, and our upper limit of potential difference, $\Delta\Psi = 4.2$ V. In the ion density profiles in Figure 6, the total ion density is given as a black dashed and double dotted line, the cation density is given as a blue dashed line, anion density is given as a red dashed-dotted line, and the density of Li$^+$ is given as a solid green line. Furthermore, we present only neat and Li-doped [pyr14][TFSI] in Figure 6 as the prototypical case for all of our electrolytes, with the few differences in EDL structure between the electrolytes being explicitly mentioned. The full ion density profiles for [pyr13][FSI] and [EMIM][BF$_4$] can be found in Figures S1 and S2, respectively, of the supporting information.[99]

For the case of $\Delta\Psi = 0$, as shown in Figure 6 a, there is a reasonable degree of fluctuation in $\rho(\Delta\mathrm{z})$ near the surface, which drops off to bulk densities at $\Delta\mathrm{z}\sim$15 nm. The density fluctuations under no potential bias imply that the layer of ions at the surface is enriched in either cations or anions, which will be later characterized by looking at surface ion populations.

The density fluctuations under no potential bias could represent the response to ion ordering or enrichment in a preferred ion at the electrode surface. In this respect, we note that the surface ions should be encompassed within the first minimum in total ion density, which is $< 5 - 7$ Å, depending on the liquid. The addition of Li-salt, as shown in Figure 6 b, results in only nominal changes to the surface ion layer. In fact, there is practically no trace of Li^+ within the surface ion layer itself, although a strong, though asymmetric, peak is present in the second ion layer near the interface of the first and second layers, occurring between 4-10 Å. This is in qualitative agreement with trends noted from previous MD simulations of the EDL of organic and ionic liquid electrolytes,[62,77] with strong solvation effects presenting a barrier to Li^+ entering the surface layer. This also reinforces the previously mentioned independence of $\langle\Psi\rangle^0$ to Li-doping, as the surface layer nearest the electrode is relatively unchanged. Aside from the peak in the second ion layer, Li^+ is distributed almost evenly throughout the Δz>10 Å region. The slight variations in Li^+ density in this region, as can be noted clearly in the total ion density profile, are due to strong and long-lived Li^+/Anion binding and network formation noted in previous works.[78,79]

The segregation of cations and anions into distinct layers and the densification of the layers in close proximity to the cathode is shown in the density profiles of Figure 6 c and d. In the case of the neat liquid in Figure 6 c, we see the surface ion layer is predominantly composed of anions, which leads to strong fluctuations in density that drop off to the bulk density by Δz∼25 Å, though small fluctuations in density can be seen to persist up to 50 Å. The addition of Li-salt disrupts layering in the EDL, leading to an uneven total ion density profile, as shown in Figure 6 d. As with the $\Delta\Psi = 0$ V case, Li^+ is again asymmetrically distributed within the second ion layer, being preferentially localized nearer to the first layer, and is not present in the first ion layer. For [pyr14][TFSI] in Figure 6 c and [pyr13][FSI] in Figure S1 c, beyond this localization a region void of Li^+ develops at $\Delta z \sim 8 - 14$ Å, followed by a diffuse accumulation at 15-25 Å. For [EMIM][BF_4], shown in Figure S2 c, this void region is not present, and, aside from the initial peak in the second ion layer, Li^+

appears to be evenly distributed through the EDL.

Ionic liquids near the anode exhibit a layered order akin to that at cathode, as shown in Figure 6 e and f, with primarily cations in the surface ion layer. For the neat system, as shown in Figure 6 e, the fluctuations in ion density again dissipate after Δz∼25 Å, with the exception being the long range fluctuations of [pyr13][FSI] that dissipate after $\Delta z \sim 40$ Å, as shown in Figure S1 e. As can be clearly noted, the second ion layer, which here is a cation layer, is more prominent than the second ion layer at the cathode. The introduction of Li-salt, given in Figure 6 f, disrupts the long-range ordering of ions and leads to abrupt peaks in the total ion density that suggest a large accumulation of Li^+ in the EDL. In this case it appears that Li^+ is asymmetrically distributed with a preference for residing near the interface of the second and third ion layers. Additionally, we see the previously noted trend of no Li^+ in the surface ion layer. Instead, and for all three liquids (Figure S1 f and S2 f), the Li^+ density is localized primarily within the anion layers, and each anion layer has an associated localization of Li^+ density. Altogether the EDL at the anode appears to have more Li^+ concentration than at the cathode. To elaborate on the structures and energetic trends noted here, we later investigate the bonding and free energetics of Li^+ in the double layer.

Surface Ion Layer

To provide a more descriptive measure of surface structure behavior beyond the global ion density profiles, we now focus on the molecular ion layer at the surface itself. We define this layer based on the density of the ion centers of mass, shown in Figures S3-S5 of the supplemental material,[99] with the initial accumulation of ions occurring within 4-6 Å for all of our electrolytes across the range of $\Delta\Psi$ probed here. To understand the composition of this layer, we compute the average surface ion density (N) attributed to this layer as a function of $\langle\Psi\rangle - \langle\Psi\rangle^0$. The value of N is determined from the product of the integral of the aforementioned density profiles of ion centers of mass from the electrode surface to the first minimum with the surface area of the electrode, and this procedure is performed for both cations and anions, with the results being shown in Figure 7 a, c, and e.

The value of N for the three liquids displays the same general behavior of more cations at lower potential and more anions at higher potential; however, there are various nuances that should be noted. At $\langle\Psi\rangle^0$, we see that [pyr14][TFSI] and [pyr13][FSI] have more cations in the surface layer, while [EMIM][BF_4] has almost an equal number of each ion. This suggests better packing of the pyrrolidinium cations with the graphite surface than the imide anion interactions, possibly through more configurational freedom. The near equal amount of [BF_4] and [EMIM] at the surface could be attributed to their relatively simple structures and similar, small size. At the extreme of negative potential, $\langle\Psi\rangle \sim -2$ V, the population of [TFSI] and [FSI] at the surface is near negligible, while [BF_4] has only been reduced to half its value at $\langle\Psi\rangle^0$. On the other hand, at $\langle\Psi\rangle \sim 2$ V we see a mixture of anions and, persistently, cations at the surface for all three liquids. The addition of Li^+ salt has limited effect on the value of N, which agrees with the ion density profiles showing no significant Li^+ density in the surface ion layer. Finally, the average number of ions in the surface layer increases with decreasing ion size, with N in [EMIM][BF_4] > [pyr13][FSI] > [pyr14][TFSI].

It has been determined previously that the surface layer governs the shape of differential capacitance.[61,74,75] To connect C_{dl} to the number of ions in the surface layer, we look at the change in surface ion density, δN, as a function of $\langle\Psi\rangle$. In this respect, we define δN as $(\langle\Psi\rangle - \langle\Psi\rangle^0)/|\langle\Psi\rangle - \langle\Psi\rangle^0|(N^- - N^+ - N_0^- + N_0^+)$, which yields the net accumulation of anions and removal of cations at the cathode and *vice versa* for the anode. This measure provides a pseudo-parabolic curve, as shown in Figure 7 b, d, and f, that reveals an interesting asymmetry for the considered electrolytes. In the case of [pyr14][TFSI], we see that the value of δN at the maximum positive potential is larger than at the minimum negative potential, which concurs with our finding that C_{dl} is larger at positive potentials for [pyr14][TFSI]. For [pyr13][FSI], we see the opposite asymmetry, with δN reaching larger values at negative potential, which again agrees with the previously noted larger values of C_{dl} at negative potentials, as well as the findings of previous simulations on [FSI] containing ionic liquids.[75] For [EMIM][BF_4], we note a nearly symmetric δN curve that coincides with a symmetric differential capacitance. As with N, the addition of Li-salt does not significantly change the trends in δN.

As a means of understanding the structural origin of changes in N and δN with potential, we look to the molecular configuration of cations and anions in the surface ion layer as a function of $\langle\Psi\rangle - \langle\Psi\rangle^0$, with representative configurations being shown in Figure S7. We first look at the distribution of the angle between the cation ring normal and the electrode surface normal, given in Figure S8. In this respect, we find that the cations at the surface can take one of two distinct states: a low angle state having the ring interact with the surface (denoted planar) and a high angle state more likely to have the chain interact with the surface (denoted perpendicular). For [pyr14], [pyr13], and [EMIM], we find the average angle of planar cations to be $\sim 8^o$, $\sim 35^o$, and $\sim 7^o$, respectively. Perpendicular cations are separated from planar cations by a minimum in the angle configuration space and are diffusely distributed through angles $> 30^o$ and $> 45^o$ for [pyr14] and [pyr13], respectively. [EMIM] does not have a clearly preferred perpendicular state; so we define perpendicular as $> 30^o$, which separates planar cations from larger angles (see Figure S8).

Mapping out the percent of planar cations in the ion surface layer as a function of potential, we see that [EMIM] is $\sim 67\%$ planar, a value virtually independent of $\langle\Psi\rangle$. On the other hand [pyr14] and [pyr13] have few planar cations at low potential ($\sim$16-20 %), which rapidly increases to almost 50 % planar at our lowest potential. Again, there are no large systematic differences between neat systems and those having Li^+. The prevalence of [pyr14] and [pyr13] at the surface across the range of potential, as given by N, is due to their two favorable states. The planar configuration, which exposes the positive charge center of the ring to the surface, is favorable at the anode, while the perpendicular configuration, which allows the cation to remain in the surface ion layer without having its charge center exposed to the electrode, is favored at the cathode. Alternatively, [EMIM] predominantly assumes a planar configuration with a positive charge center exposed to the electrode. While this configuration at the anode is favorable, the prevalence of [EMIM] at the cathode is anomalous. We therefore look to the behavior of the companion anion, [BF_4], to further understand the composition of the surface layer. The ion density profile of [EMIM][BF_4] at the cathode, given in Figure S2 c, shows that the surface layer is composed of a planar [EMIM] layer between two [BF_4] layers. The relatively small size of [BF_4] and high planarity of [EMIM] allows these ions to coexist and form a finer secondary layering of charge, or sub-layer of charge, within the surface ion layer.

Surface anions can be treated in a similar manner to the surface cations. For [TFSI] and [FSI], we use the deviation of the angle between the vector connecting the two S atoms in the S-N-S bridge from the surface normal as our gauge of configuration. For [BF_4], we employ a dynamic measure of configuration, where the vector between the most distant F-atom and the central B atom with respect to the surface is used. For [TFSI] and [FSI], we see that the anions have a high angle state where the anion lies flat on the surface (denoted flat) and a low angle configuration where the end of the anion interacts with the surface (denoted perpendicular). Likewise, the [BF_4] anions assume configurations with three F-atoms close to the surface (flat) and those with one or two F-atoms close to the surface (perpendicular). As shown in Figure S9, the anion angle distribution has a separation such that values $> 53^o$ are considered flat for both [TFSI] and [FSI] and angles $< 33^o$ are considered flat for [BF_4].

As seen from the Figure 8, the percent of flat anions increases as a function of increasing potential. At $\langle\Psi\rangle^0$, [TFSI] and [FSI] have overall high percents of flat anions ($\sim$75 %) that increases to 90-98 % at high $\langle\Psi\rangle$. The [BF_4] anion increases from roughly 50 % flat at low potential to 80 % at high potential. Both the [TFSI] and [FSI] anions assume predominantly flat configurations at the electrode surface, as previously noted with other potentials[61] and shown pictorially in Figure S7. These anions do not have a highly favorable perpendicular conformation that moves the negative charge center away from the electrode, with the negative O and F atoms on the outer shell of the molecules. This is the most likely cause of their rapid exodus from the anode with decreasing potential, as noted from N in Figure 7. Again owing primarily to its small size, the [BF$_4$] anion can closely crowd the predominantly planar [EMIM] cations and incorporate itself into the surface ion layer at the anode, leading to high value of N for [BF$_4$] at negative potenital; this is supported by the high density close to the anode given in Figure S2 e.

We see, then, that the C$_{\mathrm{dl}}$ of the three liquids can be closely related to the net change of surface ion density, δN, as a function of potential, with higher values implying higher values of capacitance. For [pyr14][TFSI], there are more cations than anions in the $\langle \Psi \rangle^0$ layer, and the present anions assume a flat configuration at the electrode surface. As the potential is decreased, the flat anions, having negative charge exposed to the electrode, are rapidly depleted from the surface, while the cation population at the surface does not dramatically increases but, rather, favors the transition of present cations to have more planar character. The loss of the few [TFSI] and the addition of few cations lead to an altogether muted change in δN. At positive potentials, however, there is a steady loss of [pyr14] and a steady gain in [TFSI] anions that lead to a net larger increase in δN when compared to negative potentials. While structurally similar though smaller than [pyr14][TFSI], [pyr13][FSI] has a larger number of both cations and anions in the $\langle \Psi \rangle^0$ layer. While [FSI] also assumes primarily flat configurations, their number in the surface layer is suitably large to sustain a high-rate of anion exit from the anode across our values of $\Delta\Psi$, leading to a larger value of δN at negative potentials when compared to positive potentials. Finally, [EMIM][BF$_4$] has a highly planar cation and a small anion that both lead to thin molecular surface layers that can be closely crowded by their counter-ions. This leads to reordering of the molecules to create a sub-layering of charge within the ion surface layer being preferred to the rapid gain or removal a given ion, which results in similar value of δN at both the anode and cathode.

Potential of Zero Charge

An important property related to the structure of the EDL is the potential of zero charge, which we have previously denoted as $\langle \Psi \rangle^0$. It is instructive to briefly describe $\langle \Psi \rangle^0$ in the context of the total electrostatic potential profile in our interfacial systems at $\Delta\Psi = 0$ V, shown in Figure S7 of the supplemental material.[99] The electrostatic potential is practically constant about $z = 0$, where the electrolyte is bulk-like in character, and we thereby refer to this potential as the bulk potential, $\langle \Psi \rangle^{\mathrm{B}}$. Alternatively, the potential as z approaches the electrode deviates from $\langle \Psi \rangle^{\mathrm{B}}$ due to the influence of the interfacial structure. Because our electrodes are identical, $\langle \sigma \rangle = 0$ when $\Delta\Psi = 0$, and the potential felt by both electrodes is potential of zero charge, $\langle \Psi \rangle^0$. In general, $\langle \Psi \rangle^0$ need not be equivalent to $\langle \Psi \rangle^{\mathrm{B}}$, as potential of the electrode is highly influenced by ion ordering at the surface.

We provide measures of both $\langle \Psi \rangle^0$ and $\langle \Psi \rangle^{\mathrm{B}}$ in Table 3. At $\mathrm{x_{Li}} = 0.0$, the values of $\langle \Psi \rangle^0$ are small and negative for [pyr14][TFSI] and [pyr13][FSI], measuring -0.06 and -0.11 V, respectively. The value for [EMIM][$\mathrm{BF_4}$], on the other hand, is positive, 0.01 V, though close to zero. The sign of $\langle \Psi \rangle^0$ for each liquid can be related to the surface ion configuration, shown in Figure 8. At $\Delta\Psi = 0$ V, both [pyr14][TFSI] and [pyr13][FSI] have a large population, ∼70-80%, of flat surface anions with negative charge centers near the electrode surface and a relatively low population, ∼15-20%, of planar cations with positive charge centers near the electrode surface. This leads to the net negative biasing of the electrode, and thus a negative potential of zero charge, at $\Delta\Psi = 0$ V. The opposite is true for [EMIM][$\mathrm{BF_4}$]. Roughly 70% of [EMIM] cations are in a planar configuration, while only ∼50% of the [$\mathrm{BF_4}$] anions are flat. This leads to the net positive biasing of the electrode, and thus a slightly potential of zero charge, at $\Delta\Psi = 0$ V.

The bulk potentials for our electrolytes are -0.79 V, -0.01 V, and -0.21 V for neat [pyr14][TFSI], [pyr13][FSI], and [EMIM][$\mathrm{BF_4}$], respectively. Interestingly, the addition of Li-salt has little influence on $\langle \Psi \rangle^0$, while its influence on the bulk potential for all electrolytes is more pronounced, with $\langle\Psi\rangle^{\mathrm{B}}$ increasing by roughly 0.1-0.2 V. The decoupling of $\langle\Psi\rangle^{0}$ and $\langle\Psi\rangle^{\mathrm{B}}$ under Li-doping implies that Li^{+} does not strongly perturb the charge density directly above the electrode surface.

Distribution and Solvation of Li^{+}

Li^{+} Distribution

We now provide a more detailed analysis of the interaction of Li^{+} with EDL structure by mapping out the net ion density ($\Delta\rho \equiv \rho^{+} - \rho^{-}$) as a function of distance from the electrode and surface potential, as given in the color maps in Figure 9 d-f. A net abundance of cations is denoted by the blue region, while a net abundance of anions is given by red regions. In additional to this, the density of Li^{+} (ρ^{Li}) is given in Figure 9 g-i. For the liquids having $\mathrm{x}_{\mathrm{Li}} = 0$, the double layer structure is clearly visible. The addition of Li^{+} leads to more disorder in the layers adjacent to the first ion layer. This is particularly notable in the second ion layer, which has greater positive character at negative potentials than the case of the neat liquid. The origin of this effect can be understood though ρ^{Li} in Figure 9 g-i, where there is a strongly localized Li^{+} signature in the second ionic layer. For larger values of Δz, the density of Li^{+} is less localized, with weak signatures appearing in more distant cation and anion layers. The surface ion layer, on the other hand has a negligible signature of Li^{+}, and such behavior explains the previously noted insensitivity of the surface ion layer properties to Li-salt doping.

To qualitatively understand the aggregation of Li^{+} in the second ionic layer, we look to the solvation structure, which is shown in Figure 10 for the representative case of [pyr14][TFSI] at the positive and negative electrodes. Against the anode, as shown in Figure 10 a, Li^{+} is solvated primarily in the second ion layer, composed of anions. As a result, a positive contribution is added into the second anion layer, which results in the second ion layer having a greater cation contribution, as noted in Figure 9 d-f. At the cathode, as displayed in Figure 10 b, we see that Li^+ resides again in the second ion layer, composed of cations. In this case, the anions bond to Li^+ across the second cation layer. The majority of binding anions originate from the first ion layer, with the remainder being from the third ion layer. In all cases, we note that Li^+ maintains 4-coordinated, atomically, solvation structure in a similar manner to bulk systems.[79] Energetically speaking, against the anode Li^+ must remain in the second anion layer due to the strong Li/Anion binding, while against the cathode Li^+ remains in the second cation layer due to a balance between a strong repulsion to the cathode and sufficient binding from the first and third anion layers. One would expect such binding to create a barrier to the translation of Li^+ through the EDL surface ion layer.

Li^+ Solvation Free Energy

We first focus on obtaining the solvation free energy of Li^+ in the $z = 0$ plane in the bulk region of the electrolyte at $\Delta\Psi = 0$ V, the values of which are given in Table 4 for the three electrolytes of interest in the present work. The first step of the thermodynamic cycle takes neutral Li^0 from the gas phase to a solvated state in the $z = 0$ plane of our model capacitor. This step of the cycle yields $\Delta F^{\mathrm{Li}^0(g)\rightarrow\mathrm{Li}^0(l)}$ values of 4.2, 4.7 and 4.6 kcal/mol for [pyr14][TFSI], [pyr13][FSI], and [EMIM][BF_4], respectively. The solvated Li^0 interacts with the ionic liquid only through repulsive-dispersive interactions, which are unfavorable with respect to the transition from the gas phase as seen from the positive contributions to the solvation free energy. The second step of the cycle involves the charging of solvated Li^0 to Li^+ while simultaneously counter charging an electrode to -1 a.u. The Li^+ solvation free energy contribution from this leg of the cycle $\Delta F^{\mathrm{Li}^0(l)\rightarrow\mathrm{Li}^+(l)}$, which can be resolved by removing ΔF^{edl} according to Fig. 5, is -105.8, -105.5, and -101.9 kcal/mol for [pyr14][TFSI], [pyr13][FSI], and [EMIM][BF_4], respectively. The electrostatic interactions introduced by this transition are favorable to solvation and of an order of magnitude larger than the repulsive-dispersive contribution, leading to a highly favorable values of ΔF^s.

Concerning the magnitude of F^s shown in Table 4, our values are in general agreement with previous measures of the solvation of other elemental, monovalent cations into aqueous solutions.[100] The value of F^s for the three electrolytes follows the order [pyr14][TFSI] < [pyr13][FSI] < [EMIM][BF$_4$], which interestingly follows the trend of Li$^+$ ionic conductivity and the inverse trend of anion size.[79] There is not strictly speaking a previously established correlation between F^s and Li$^+$ conductivity, though one could suppose that a more weakly solvated ion would have increased mobility.

With the solvation free energy of Li$^+$ into the bulk in hand, we can now determine the solvating free energy as a function of distance from the electrode at different values of $\Delta\Psi$. In this case, we employ our standard two electrode setup with a given value of $\Delta\Psi$ applied between the electrodes, perform MD simulations with Li$^+$ constrained to various z-planes throughout the EDL, and populate the solvation free energy using the "blue-moon" ensemble as represented by Eq. 12. The resulting free energies profiles, given in terms of distance from the electrode surface $F^s(\Delta z)$, are shown in Fig. 11 for $\Delta\Psi$ values of 0 V and 4.2 V. The free energy profiles are in line with our expectations from the distribution of Li$^+$ given in Figure 9 and provide a comparative quantification of barriers to Li$^+$ transport in the EDLs of the different electrolytes. At the neutral electrode, $\Delta\Psi = 0$ V, we see a 5 kcal/mol barrier to Li$^+$ motion from $\Delta z = 7$ Å to 5 Å for [pyr14][TFSI], corresponding to motion from the second molecular layer to the surface ion layer. Such a barrier is not present in the other electrolyte systems. We can trace this barrier to the fact that, as shown in Figure 7, [pyr14][TFSI] has a highly cation enriched surface layer that would be unfavorable to Li$^+$ solvation. Intercalating Li$^+$ with its solvation shell of large [TFSI] anions is also an unfavorable contribution to translation into the surface ion layer.

Upon applying a potential difference between the electrodes of $\Delta\Psi = 4.2$ V, we find some consistent trends between the three liquids at the negative electrode. Namely, a 7-8 kcal/mol barrier to Li$^+$ motion from $\Delta z = 7$ Å to 5 Å evolves for all electrolytes. As with the neutral electrode with [pyr14][TFSI], this corresponds to motion from the second molecular layer to the surface ion layer. As the second molecular layer is primarily anions at the negative electrode, it is highly favorable for Li^+ to remain in this layer, hence the barrier to insertion into the surface ion layer.

Alternatively, at the positive electrode of the system having $\Delta\Psi = 4.2$ V, we see slightly different behavior between the three liquids. For [pyr14][TFSI] and [EMIM][BF_4], a minimum in F^s evolves around Δz values of 4-5 Å, and a maximum evolves around 8-10 Å, with the difference between the extrema being 5 kcal/mol and 6 kcal/mol for [pyr14][TFSI] and [EMIM][BF_4], respectively. For [pyr13][FSI], on the other hand, the minimum is clearly present, but the maximum is much lower than the other liquids, leading to a difference between the extrema of 2.5 kcal/mol.

For all three electrolytes, the minimum is a reflection of Li^+ preferring to remain at the interface of the anion-rich surface layer and the cation rich second molecular layer. For example, as can be seen in Figure 10 b, Li^+ remains 4-coordinated with 3 O atoms from the surface ion layer and a monodentate [TFSI] drawn from the third molecular layer, which represent the free energy well at 4-5 Å. The binding of Li^+ with an anion in the third molecular layer across the adjacent cation layer is unfavorable as it disrupts the segregation of charge, and the optimum structure mitigates this by requiring only one anion to be inserted into the layer.

Concerning the maximum in free energy, as Li^+ is forced into the second molecular layer (cation layer) at the positive electrode, its solvating anions are introduced into this layer too. This is unfavorable and leads to the noted increase in free energy around the 8-10 Å region. The specific solvation structure of Li^+ in each electrolyte, however, changes the magnitude of the noted maximum. The solvation structure of a Li^+ constrained to reside at the maximum of free energy is shown in Figure 12. For [pyr14][TFSI], we see a surface anion bound to Li^+ in a monodentate configuration as well as anions originating from the third molecular layer bound in monodentate and bidentate configurations. The same anion binding configuration is noted for [EMIM][BF_4], which is unusual as Li^+ prefers 4 monodentate [BF_4] bond in the bulk electrolyte. The small size of the anions leads to all three being incorporated into the cation layer, which is highly unfavorable. Both of these solvation structures lead to the similar energetic barriers to Li^+ translation. On the other hand, [pyr13][FSI] has a much lower maximum, with Li^+ assuming a solvation shell having 4 monodentate anions. The anions in this case, as seen in Figure 12, are all monodentate, which leads to their negative charge centers being more removed from the cation layer. This reduces the energetic cost of inserting Li^+ into the cation layer.

Conclusions

In the present work we investigate the influence of Li-salt doping on the electric double layer formation and capacitance of three ionic liquids ([pyr14][TFSI], [pyr13][FSI], and [EMIM][BF_4]) at 363 K and for $0 \leq$ V $\Delta\Psi \leq 4.2$ V. To represent the interfaces, we use a dual electrode model, one being the positive and the other being the negative electrode, with a potential difference imposed on the electrode through the constant-$\Delta\Psi$ method. Beyond typical computations of this nature, the interfaced electrolyte is represented with a polarizable force field, which has been shown previously to ensure accurate ion density and alignment at electrified interfaces.[85] The differential capacitance is computed using a newly derived fluctuation formula that yields capacitance as a function of surface potential. The fluctuation formula is shown to be an effective method to compute differential capacitance, and further avoids the computational overhead of taking a direct derivative of surface charge with respect to surface potential, which requires many simulations over a fine $\Delta\Psi$ grid to achieve an accurate result.

While all three liquids have similar EDL formation rates, we see that [pyr13][FSI] has slightly better overall energy storage characteristics, or lower EDL formation free energy, than [pyr14][TFSI] or [EMIM][BF_4]. Concerning our computations using ideal metallic electrodes, all three liquids exhibit asymmetric differential capacitance about the potential of zero charge. This is in line with the expected camel-shaped profiles previously observed in experimental measurements of ionic liquids at metallic electrodes. The addition of Li-salt to our systems leads to a decrease in asymmetry, likely as a result of the disorder Li^+ introduces into the electric double layer structure. For our experimental measurements on glassy carbon electrodes, differential capacitance adopts a U-like profile and has a larger magnitude than our computational results. The differences between theoretical predictions and experiment underscore the strong influence of electrode surface structure and pseudocapacitive effects on differential capacitance.

We have mapped out the electric double layer structure, noting the expected alternating layers of cations and anions from previous studies. The introduction of Li^+ leads to EDL disorder, which is observable in the differential capacitance as well as the ion density profiles. One particular aspect of the EDL that is not strongly influenced by the introduction of Li^+ is the composition and structure of the first molecular layer of ions at the surface. We find that the behavior of the surface ions imparts a great deal of information about the differential capacitance, namely in describing the overall shape of this quantity. For instance, we find that regions of higher differential capacitance correspond to greater ion buildup at the surface and a corresponding alignment that leads to more dense packing.

We have also investigated the distribution of Li^+ in the double layer as a function of potential and have found a strong localization behavior in the second ion layer of the EDL. At the anode, the localization is a result of the strong anion binding in the second molecular layer, while at the cathode Li^+ resides in the second cation layer and forms bonds with both the first and third anion layers. Quantifying this behavior, we have performed an in-depth study of free energy of Li^+ in the electric double layer. We compute the free energy of Li^+ solvation into the bulk-like region in our model capacitor and perform constrained dynamics as a function of distance from the electrode to understand solvation free energetic difference in the double layer. We note that solvation free energy follows the trend of [pyr14][TFSI] $<$

[pyr13][FSI] < [EMIM][BF_4], which is inverse to the size of solvating anions. For electrodes having a $\Delta\Psi$ of 0 V, [pyr14][TFSI] exhibits a 5 kcal/mol barrier to Li^+ translation to the surface ion layer, which originates from cation enrichment of this layer at neutral conditions. This barrier is not present in the other electrolytes. Concerning the negative electrode of a system having a $\Delta\Psi$ of 4.2 V, a barrier to Li^+ insertion into the surface layer occurs due to favorable anion solvation in the second molecular layer. On the positive electrode, a well forms near the anion layer at the surface again due to strong Li/anion interactions. Interestingly, the solvation structure of Li^+ in the liquids leads to different free energy barriers, with [pyr13][FSI] exhibiting the smallest barrier due to a more diffuse solvation structure.

Acknowledgement

This work was supported by funding from the NASA Aeronautics Research Institute (NARI) Seedling program.

References

(1) Armand, M.; Endres, F.; MacFarlane, D. R.; Ohno, H.; Scrosati, B. Ionic-Liquid Materials for the Electrochemical Challenges of the Future. *Nature Mater.* **2009**, *8*, 621–629.

(2) Buzzeo, M. C.; Evans, R. G.; Compton, R. G. Non-Haloaluminate Room-Temperature Ionic Liquids in Electrochemistry - A Review. *ChemPhysChem* **2004**, *5*, 1106–1120.

(3) Fedorov, M. V.; Kornyshev, A. A. Ionic Liquids at Electrified Interfaces. *Chem. Rev.* **2014**, *114*, 2978–3036.

(4) Simon, P.; Gogotsi, Y. Materials for Electrochemical Capacitors. *Nature Mater.* **2008**, *7*, 845–854.

(5) Lockett, V.; Horne, M.; Sedev, R.; Rodopoulos, T.; Ralston, J. Differential Capacitance of the Double Layer at the Electrode/Ionic Liquids Interface. *Phys. Chem. Chem. Phys.* **2010**, *12*, 12499–12512.

(6) Alam, M. T.; Islam, M. M.; Okajima, T.; Ohsaka, T. Measurements of Differential Capacitance at Mercury/Room-Temperature Ionic Liquids Interfaces. *J. Phys. Chem. C* **2007**, *111*, 18326–18333.

(7) Lockett, V.; Sedev, R.; Ralston, J.; Horne, M.; Rodopoulos, T. Differential Capacitance of the Electrical Double Layer in Imidazolium-Based Ionic Liquids: Influence of Potential, Cation Size, and Temperature. *J. Phys. Chem. C* **2008**, *112*, 7486–7495.

(8) Zheng, J.; Moganty, S. S.; Goonetilleke, P. C.; Baltus, R. E.; Roy, D. A Comparative Study of the Electrochemical Characteristics of [Emim$^+$][BF$_4^-$] and [Bmim$^+$][BF$_4^-$] Ionic Liquids at the Surfaces of Carbon Nanotube and Glassy Carbon Electrodes. *J. Phys. Chem. C* **2011**, *115*, 7527–7537.

(9) Zheng, J. P.; Goonetilleke, P. C.; Pettit, C. M.; Roy, D. Probing the Electrochemical Double Layer of an Ionic Liquid Using Voltammetry and Impedance Spectroscopy: A Comparative Study of Carbon Nanotube and Glassy Carbon Electrodes in [EMIM]$^+$[EtSO$_4$]$^-$. *Talanta* **2010**, *81*, 1045–1055.

(10) Drüschler, M.; Huber, B.; Passerini, S.; Roling, B. Hysteresis Effects in the Potential-Dependent Double Layer Capacitance of Room Temperature Ionic Liquids at a Polycrystalline Platinum Interface. *J. Phys. Chem. C* **2010**, *114*, 3614–3617.

(11) Xu, J.; Yang, J.; NuLi, Y.; Wang, J.; Zhang, Z. Additive-Containing Ionic Liquid Electrolytes for Secondary Lithium Battery. *J. Power Sources* **2006**, *160*, 621–626.

(12) Wang, H.; Liu, S.; Huang, K.; Yin, X.; Liu, Y.; Peng, S. BMIMBF$_4$ Ionic Liquid Mixtures Electrolyte for Li-Ion Batteries. *Int. J. Electrochem. Sci.* **2012**, *7*, 1688–1698.

(13) Bhattacharyya, R.; Key, B.; Chen, H.; Best, A. S.; Hollenkamp, A. F.; Grey, C. P. *In Situ* NMR Observation of the Formation of Metallic Lithium Microstructures in Lithium Batteries. *Nat. Mater.* **2010**, *9*, 504–510.

(14) Schweikert, N.; Hofmann, A.; Schulz, M.; Scheuermann, M.; Boles, S. T.; Hanemann, T.; Hahn, H.; Indris, S. Suppressed Lithium Dendrite Growth in Lithium Batteries Using Ionic Liquid Electrolytes: Investigation by Electrochemical Impedance Spectroscopy, Scanning Electron Microscopy, and *In Situ* ^{7}Li Nuclear Magnetic Resonance Spectroscopy. *J. Power Sources* **2013**, *228*, 237–243.

(15) Howlett, P. C.; MacFarlane, D. R.; Hollenkamp, A. F. High Lithium Metal Cycling Efficiency in a Room-Temperature Ionic Liquid. *Electrochem. Solid State Lett.* **2004**, *7*, A97–A101.

(16) Matsumoto, H.; Sakaebe, H.; Tatsumi, K.; Kikuta, M.; Ishiko, E.; Kono, M. Fast Cycling of Li/$LiCoO_2$ Cell with Low-Viscosity Ionic Liquids Based on Bis(Fluorosufonyl)Imide ($[FSI]^-$). *J. Power Sources* **2006**, *160*, 1308–1313.

(17) Basile, A.; Hollenkamp, A. F.; Bhatt, A. I.; O'Mullane, A. P. Extensive Charge-Discharge Cycling of Lithium Metal Electrodes Achieved Using Ionic Liquid Electrolytes. *Electrochem. Commun.* **2013**, *27*, 69–72.

(18) Naoi, K. 'Nanohybrid Capacitor': The Next Generation Electrochemical Capacitors. *Fuel Cells* **2010**, *10*, 825–833.

(19) Lin, R.; Huang, P.; Ségalini, J.; Largeot, C.; Taberna, P. L.; Chmiola, J.; Gogotsi, Y.; Simon, P. Solvent Effect on the Ion Adsorption from Ionic Liquid Electrolyte into Sub-Nanometer Carbon Pores. *Electrochim. Acta* **2009**, *54*, 7025–7032.

(20) Li, S.; Van Aken, K. L.; McDonough, J. K.; Feng, G.; Gogotsi, Y.; Cummings, P. T. The Electrical Double Layer of Dicationic Ionic Liquids at Onion-like Carbon Surface. *J. Phys. Chem. C* **2014**, *118*, 3901–3909.

(21) Centeno, T. A.; Sereda, F., O. Stoeckli Capacitance in Carbon Pores of 0.7 to 15 nm: A Regular Pattern. *Phys. Chem. Chem. Phys.* **2011**, *13*, 12403–12406.

(22) Largeot, C.; Portet, C.; Chmiola, J.; Taberna, P.-L.; Gogotsi, Y.; Simon, P. Relation between the Ion Size and Pore Size for an Electric Double-Layer Capacitor. *J. Am. Chem. Soc.* **2008**, *130*, 2730–2731.

(23) Wu, P.; Huang, J.; Meunier, V.; Sumpter, B. G.; Qiao, R. Complex Capacitance Scaling in Ionic Liquids-Filled Nanopores. *ACS Nano* **2011**, *5*, 9044–9051.

(24) Bedrov, D.; Vatamanu, J.; Hu, Z. Ionic Liquids at Charged Surfaces: Insight from Molecular Simulations. *J. Non-Cryst. Solids* **2014**, in press.

(25) Feng, G.; Cummings, P. T. Supercapacitor Capacitance Exhibits Oscillatory Behavior as a Function of Nanopore Size. *J. Phys. Chem. Lett.* **2011**, *2*, 2859–2864.

(26) Shim, Y.; Kim, H. J. Nanoporous Carbon Supercapacitors in an Ionic Liquid: A Computer Simulation Study. *ACS Nano* **2010**, *4*, 2345–2355.

(27) Merlet, C.; Rotenberg, B.; Madden, P. A.; Taberna, P.-L.; Simon, P.; Gogotsi, Y.; Salanne, M. On the Molecular Origin of Supercapacitance in Nanoporous Carbon Electrodes. *Nature Mater.* **2012**, *11*, 306–310.

(28) Jiang, D.; Jin, Z.; Wu, J. Oscillation of Capacitance inside Nanopores. *Nano Lett.* **2011**, *11*, 5373–5377.

(29) Vatamanu, J.; Vatamanu, M.; Bedrov, D. Non-Faradic Energy Storage by Room Temperature Ionic Liquids in Nanoporous Electrodes. *ACS Nano* **2015**, *Just Accepted*, Just Accepted.

(30) Su, Y.-Z.; Fu, Y.-C.; Yan, J.-W.; Chen, Z.-B.; Mao, B.-W. Double Layer of Au(100)/Ionic Liquid Interface and Its Stability in Imidazolium-Based Ionic Liquids. *Angew. Chem. Int. Ed.* **2009**, *48*, 5148–5151.

(31) Islam, M. M.; Alam, M. T.; Ohsaka, T. Electrical Double-Layer Structure in Ionic Liquids: A Corroboration of the Theoretical Model by Experimental Results. *J. Phys. Chem. C* **2008**, *112*, 16568–16574.

(32) Alam, M. T.; Islam, M. M.; Okajima, T.; Ohsaka, T. Ionic Liquid Structure Dependent Electrical Double Layer at the Mercury Interface. *J. Phys. Chem. C* **2008**, *112*, 2601–2606.

(33) Mezger, M.; H., S.; Reichart, H.; Schramm, S.; Okasinski, J. S.; Sch oder, S.; Honkim aki, V.; Deutsch, M.; Ocko, B. M.; Ralston, J. et al. Molecular Layering of Fluorinated Ionic Liquids at a Charged Sapphire (0001) Surface. *Science* **2008**, *322*, 424–428.

(34) Mezger, M.; Schramm, S.; H., S.; Reichart, H.; Deutsch, M.; De Souza, E. J.; Okasinski, J. S.; Ocko, B. M.; Honkim aki, V.; Dosch, H. Layering of $[\mathrm{BMIM}]^+$-based Ionic Liquids at a Charged Sapphire Interface. *J. Chem. Phys.* **2009**, *131*, 094701.

(35) Mezger, M.; Ocko, B. M.; Reichert, H.; Deutsch, M. Surface Layering and Melting in an Ionic Liquid Studied by Resonant Soft X-ray Reflectivity. *Proc. Natl. Acad. Sci.* **2013**, *110*, 3733–3737.

(36) Nishi, N.; Yasui, Y.; Uruga, T.; Tanida, H.; Yamada, T.; Nakayama, S.; Matsuoka, H.; Kakiuchi, T. Ionic Multilayers at the Free Surface of an Ionic Liquid, Trioctylmethylammonium Bis(nonafluorobutanesulfonyl)amide, Probed by X-ray Reflectivity Measurements. *J. Chem. Phys.* **2010**, *132*, 164705.

(37) Yamamoto, R.; Morisaki, H.; Sakata, O.; Shimotani, H.; Yuan, H.; Iwasa, Y.; Kimura, T.; Wakabayashi, Y. External Electric Field Dependence of the Structure of the Electric Double Layer at an Ionic Liquid/Au Interface. *Appl. Phys. Lett.* **2012**, *101*, 053122.

(38) Hayes, R.; El Abedin, S. Z.; Atkin, R. Pronounced Structure in Confined Aprotic Room-Temperature Ionic Liquids. *J. Phys. Chem. B Lett.* **2009**, *113*, 7049–7052.

(39) Wakeham, D.; Hayes, R.; Warr, G. G.; Atkin, R. Influence of Temperature and Molecular Structure on Ionic Liquid Solvation Layers. *J. Phys. Chem. B* **2009**, *113*, 5961–5966.

(40) Atkin, R.; Warr, G. G. Structure in Confined Room-Temperature Ionic Liquids. *J. Phys. Chem. C* **2007**, *111*, 5162–5168.

(41) Black, J. M.; Walters, D.; Labuda, A.; Feng, G.; Hillesheim, P. C.; Dai, S.; Cummings, P. T.; Kalinin, S. V.; Proksch, R.; Balke, N. Bias-Dependent Molecular-Level Structure of Electrical Double Layer in Ionic Liquid on Graphite. *Nano Lett.* **2013**, *13*, 5954–5960.

(42) Hayes, R.; Borisenko, N.; Tam, M. K.; Howlett, P. C.; Endres, F.; Atkin, R. Double Layer Structure of Ionic Liquids at the Au(111) Electrode Interface: An Atomic Force Microscopy Investigation. *J. Phys. Chem. C* **2011**, *115*, 6855–6863.

(43) Buchner, F.; Forster-Tonigold, K.; Bozorgchenani, M.; Gross, A.; J urgen Behm, R. Interaction of a Self-Assembled Ionic Liquid Layer with Graphite(0001): A Combined Experimental and Theoretical Study. *J. Phys. Chem. Lett.* **2016**, *7*, 226–233.

(44) Aliaga, C.; Baldelli, S. Sum Frequency Generation Spectroscopy and Double-Layer Capacitance Studies of the 1-Butyle-3-Methylimidazolium Dicyanamide-Platinum Interface. *J. Phys. Chem. B* **2006**, *110*, 18481–18491.

(45) Rivera-Rubero, S.; Baldelli, S. Surface Spectroscopy of Room-Temperature Ionic Liquids on a Platinum Electrode: A Sum Frequency Generation Study. *J. Phys. Chem. B* **2004**, *108*, 15133–15140.

(46) Baldelli, S. Probing Electric Fields at the Ionic Liquid-Electrode Interface Using Sum Frequency Generation Spectroscopy and Electrochemistry. *J. Phys. Chem. B Lett.* **2005**, *109*, 13049–13051.

(47) Santos Jr., V. O.; Alves, M. B.; Carvalho, M. S.; Suarez, P. A. Z.; Rubim, J. C. Surface-Enhanced Raman Scattering at the Silver Electrode/Ionic Liquid ($BMIPF_6$) Interface. *J. Phys. Chem. B* **2006**, *110*, 20379–20385.

(48) Nanbu, N.; Sasaki, Y.; Kitamura, F. *In Situ* FT-IR Spectroscopic Observation of a Room-Temperature Molten Salt | Gold Electrode Interphase. *Electrochem. Commun.* **2003**, *5*, 383–387.

(49) Kornyshev, A. A. Double-Layer in Ionic Liquids: Paradigm Change? *J. Phys. Chem. B* **2007**, *111*, 5545–5557.

(50) Fedorov, M. V.; Kornyshev, A. A. Ionic Liquid Near a Charged Wall: Structure and Capacitance of Electrical Double Layer. *J. Phys. Chem. B* **2008**, *112*, 11868–11872.

(51) Georgi, N.; Kornyshev, A. A.; Fedorov, M. V. The Anatomy of the Double Layer and Capacitance in Ionic Liquids with Anisotropic Ions: Electrostriction *vs.* Lattice Saturation. *J. Electroanal. Chem.* **2010**, *649*, 261–267.

(52) Ivaništšev, V.; Fedorov, M. V. Interfaces between Charged Surfaces and Ionic Liquids: Insights from Molecular Simulations. *Interface* **2014**, *23*, 65–69.

(53) Limmer, D. T. Interfacial Ordering and Accompanying Divergent Capacitance at Ionic Liquid-Metal Interfaces. *Phys. Rev. Lett.* **2015**, *115*, 256102.

(54) Black, J. M.; Okatan, M. B.; Feng, G.; Cummings, P. T.; Kalinin, S. V.; Balke, N. Topological Defects in Electric Double Layers of Ionic Liquids at Carbon Interfaces. *Nano Energy* **2015**, *15*, 737–745.

(55) Uysal, A.; Zhou, H.; Feng, G.; Lee, S. S.; Li, S.; Cummings, P. T.; Fulvio, P. F.; Dai, S.; McDonough, J. K.; Gogotsi, Y. et al. Interfacial Ionic 'Liquids': Connecting Static and Dynamic Structures. *J. Phys.:Condens. Matter* **2015**, *27*, 032101.

(56) Merlet, C.; Limmer, D.; Salanne, M.; van Roij, R.; Madden, P. A.; Chandler, D.; Rotenberg, B. The Electric Double Layer Has a Life of Its Own. *J. Phys. Chem. C* **2014**, *118*, 18291–18298.

(57) Van Aken, K. L.; McDonough, J. K.; Li, S.; Feng, G.; Chathoth, S. M.; Mamontov, E.; Fulvio, P. F.; Cummings, P. T.; Dai, S.; Gogotsi, Y. Effect of Cation on Diffusion Coefficient of Ionic Liquids at Onion-Like Carbon Electrodes. *J. Phys.: Condens. Matter* **2014**, *26*, 284104.

(58) Shim, Y.; Jung, Y.; Kim, H. J. Graphene-Based Supercapacitors: A Computer Simulation Study. *J. Phys. Chem. C* **2011**, *115*, 23574–23583.

(59) Tazi, S.; Salanne, M.; Simon, C.; Turq, P.; Pounds, M.; Madden, P. A. Potential-Induced Ordering Transition of the Adsorbed Layer at the Ionic Liquid-Electrified Metal Interface. *J. Phys. Chem. B* **2010**, *114*, 8453–8459.

(60) Lynden-Bell, R. M.; Del Pópolo, M. G.; Youngs, T. G. A.; Kohanoff, J.; Hanke, C. G.; Harper, J. B.; Pinilla, C. C. Simulations of Ionic Liquids, Solutions, and Surfaces. *Acc. Chem. Res.* **2007**, *40*, 1138–1145.

(61) Vatamanu, J.; Borodin, O.; Smith, G. D. Molecular Insights into the Potential and Temperature Dependences of the Differential Capacitance of a Room-Temperature Ionic Liquid at Graphite Electrodes. *J. Am. Chem. Soc.* **2010**, *132*, 14825–14833.

(62) Vatamanu, J.; Borodin, O.; Smith, G. D. Molecular Dynamics Simulation Studies of the Structure of a Mixed Carbonate/LiPF$_6$ Electrolyte near Graphite Surface as a Function of Electrode Potential. *J. Phys. Chem. C* **2011**, *116*, 1114–1121.

(63) Vatamanu, J.; Borodin, O.; Smith, G. D. Molecular Dynamics Simultions of Atomically Flat and Nanoporous Electrodes with a Molten Salt Electrolyte. *Phys. Chem. Chem. Phys.* **2010**, *12*, 170–182.

(64) Feng, G.; Zhang, J. S.; Qiao, R. Microstructure and Capacitance of the Electrical Double Layers at the Interface of Ionic Liquids and Planar Electrodes. *J. Phys. Chem. C* **2009**, *113*, 4549–4559.

(65) Merlet, C.; Salanne, M.; Rotenberg, B.; Madden, P. A. Imidazolium Ionic Liquid Interfaces with Vapor and Graphite: Interfacial Tension and Capacitance from Coarse-Grained Molecular Simulations. *J. Phys. Chem. C* **2011**, *115*, 16613–16618.

(66) Coasne, B.; Viau, L.; Vioux, A. Loading-Controlled Stiffening in Nanoconfined Ionic Liquids. *J. Phys. Chem. Lett.* **2011**, *2*, 1150–1154.

(67) Feng, G.; Qiao, R.; Huang, J.; Sumpter, B. G.; Meunier, V. Atomistic Insight on the Charging Energetics in Subnanometer Pore Supercapacitors. *J. Phys. Chem. C* **2010**, *114*, 18012–18016.

(68) Rajput, N. N.; Monk, J.; Singh, R.; Hung, F. R. Structure and Dynamics of an Ionic Liquid Confined Inside a Charged Slit Graphitic Nanopore. *J. Phys. Chem. C* **2012**, *116*, 14504–14513.

(69) Rajput, N. N.; Monk, J.; Singh, R.; Hung, F. R. On the Influence of Pore Size and Pore Loading on Structural and Dynamical Heterogeneities of an Ionic Liquid Confined in a Slit Nanopore. *J. Phys. Chem. C* **2012**, *116*, 5169–5181.

(70) Pinialla, C.; Del Pópolo, M. G.; Lynden-Bell, R. M.; Kohanoff, J. Structure and Dynamics of a Confined Ionic Liquid. Topics of Relevance to Dye-Sensitized Solar Cells. *J. Phys. Chem. B* **2005**, *109*, 17922–17927.

(71) Pinialla, C.; Del Pópolo, M. G.; Kohanoff, J.; Lynden-Bell, R. M. Polarization Relaxation in an Ionic Liquid Confined between Electrified Walls. *J. Phys. Chem. B* **2007**, *111*, 4877–4884.

(72) Shim, Y.; Kim, H. J. Solvation of Carbon Nanotubes in a Room-Temperature Ionic Liquid. *ACS Nano* **2009**, *3*, 1693–1702.

(73) Dong, K.; Zhou, G.; Liu, X.; Yao, X.; Zhang, S.; Lyubartsev, A. Structural Evidence for the Ordered Crystallites of Ionic Liquid in Confined Carbon Nanotubes. *J. Phys. Chem. C* **2009**, *113*, 10013–10020.

(74) Hu, Z.; Vatamanu, J.; Borodin, O.; Bedrov, D. A Comparative Study of Alkylimidazolium Room Temperature Ionic Liquids with FSI and TFSI Anions near Charged Electrodes. *Electrochim. Acta* **2014**, *145*, 40–52.

(75) Vatamanu, J.; Borodin, O.; Smith, G. D. Molecular Simulations of the Electric Double Layer Structure, Differential Capcitance, and Charging Kinetics for *N*-Methyl-*N*-Propylpyrrolidinium Bis(Fluorosulfonyl)Imide at Graphite Electrodes. *J. Phys. Chem. B* **2011**, *115*, 3073–3084.

(76) Smith, A. M.; Perkin, S. Influence of Lithium Solutes on Double-Layer Structure of Ionic Liquids. *J. Phys. Chem. Lett.* **2015**, *6*, 4857–4861.

(77) Ivaništšev, V.; Méndez-Morales, T.; Lynden-Bell, R. M.; Cabeza, O.; Gallego, L. J.; Varela, L. M.; Fedorov, M. V. Molecular Origin of High Free Energy Barriers for Alkali Metal Ion Transfer through Ionic Liquid-Graphene Electrode Interfaces. *Phys. Chem. Chem. Phys.* **2016**, *18*, 1302–1310.

(78) Bauschlicher, C. W., Jr.; Haskins, J. B.; Bucholz, E. W.; Lawson, J. W.; Borodin, O. Structure and Energetics of $\mathrm{Li^+}$-$(\mathrm{BF_4^-})_n$, $\mathrm{Li^+}$-$(\mathrm{FSI_4^-})_n$, and $\mathrm{Li^+}$-$(\mathrm{TFSI_4^-})_n$: *Ab Initio* and Polarizable Force Field Approaches. *J. Phys. Chem. B* **2014**, *118*, 10785–10794.

(79) Haskins, J. B.; Bennett, W. R.; Wu, J. J.; Hernández, D. M.; Borodin, O.; Monk, J. D.; Bauschlicher, C. W., Jr.; Lawson, J. W. Computational and Experimental Investigation of Li-doped Ionic Liquid Electrolytes: [pyr14][TFSI], [pyr13][FSI], and [EMIM][BF_4]. *J. Phys. Chem. B* **2014**, *118*, 11295–11309.

(80) Borodin, O.; Smith, G. D. Development of Many-Body Polarizable Force Fields for Li-Battery Components: 1. Ether, Alkane, and Carbonate-Based Solvents. *J. Phys. Chem. B* **2006**, *110*, 6279–6292.

(81) Borodin, O.; Smith, G. D. Development of Many-Body Polarizable Force Fields for Li-Battery Applications: 2. LiTFSI-Doped Oligoether, Polyether, and Carbonate-Based Electrolytes. *J. Phys. Chem. B* **2006**, *110*, 6293–6299.

(82) Borodin, O. Polarizable Force Field Development and Molecular Dynamics Simulations of Ionic Liquids. *J. Phys. Chem. B* **2009**, *113*, 11463–11478.

(83) Borodin, O.; D., S. G.; Henderson, W. Li^+ Cation Environment, Transport, and Mechanical Properties of the LiTFSI Doped *N*-Methyl-*N*-Alkylpyrrolidinium$^+$ TFSI$^-$ Ionic Liquids. *J. Phys. Chem. B* **2006**, *110*, 16879–16886.

(84) Li, Z.; Smith, G. D.; Bedrov, D. Li^+ Solvation and Transport Properties in Ionic Liquid/Lithium Salt Mixtures: A Molecular Dynamics Simulation Study. *J. Phys. Chem. B* **2012**, *116*, 12801–12809.

(85) Haskins, J. B.; Lawson, J. W. Evaluation of Methods for the Simulation of Ionic Liquid Electrified Interfaces. *J. Chem. Phys. (Submitted).*

(86) Solano, C. J. F.; Jeremias, S.; Paillard, E.; Beljonne, D.; Lazzaroni, R. A Joint Theoretical/Experimental Study of the Structure, Dynamics, and Li^+ Transport in Bis([tri]fluoro[methane]sulfonyl)Imide [T]FSI-Based Ionic Liquids. *J. Chem. Phys.* **2013**, *139*, 034502.

(87) Kawata, M.; Mikami, M. Rapid Calculation of Two-Dimensional Ewald Summation. *Chem. Phys. Lett.* **2001**, *340*, 157–164.

(88) Yeh, I.-C.; Berkowitz, M. L. Ewald Summation for Systems with Slab Geometry. *J. Chem. Phys.* **1999**, *111*, 3155–3162.

(89) Siepmann, J. I.; Sprik, M. Influence of Surface Topology and Electrostatic Potential on Water/Electrode Systems. *J. Chem. Phys.* **1995**, *102*, 511.

(90) Reed, S. K.; Lanning, O. J.; Madden, P. A. Electrode Interface Between an Ionic Liquid and a Model Metallic Electrode. *J. Chem. Phys.* **2007**, *126*, 084704.

(91) Carter, E. A.; Ciccotti, G.; Hynes, J. T.; Kapral, R. Constrained Reaction Coordinate Dynamics for the Simulation of Rare Events. *Chem. Phys. Lett.* **1989**, *156*, 472.

(92) Ivaništšev, V.; Fedorov, M. V.; Lynden-Bell, R. M. Screening of Ion-Graphene Electrode Interactions by Ionic Liquids: the Effects of Liquid Structure. *J. Phys. Chem. C* **2014**, *118*, 5841–5847.

(93) Fedorov, M. V.; Lynden-Bell, R. M. Probing the Neutral Graphene-Ionic Liquid Interface: Insights from Molecular Dynamics Simulations. *Phys. Chem. Chem. Phys.* **2012**, *14*, 2552–2556.

(94) Lynden-Bell, R. M.; Frolov, A. I.; Fedorov, M. V. Electrode Screening by Ionic Liquids. *Phys. Chem. Chem. Phys.* **2012**, *14*, 2693–2701.

(95) Tuckerman, M.; Berne, B. J.; Martyna, G. J. Reversible Multiple Time Scale Molecular Dynamics. *J. Chem. Phys.* **1992**, *97*, 1990.

(96) Gnahm, M.; Pajkossy, T.; Kolb, D. M. The Interface between Au(111) and an Ionic Liquid. *Electrochim. Acta* **2010**, *55*, 6212–6217.

(97) Pajkossy, T.; Kolb, D. M. The Interfacial Capacitance of Au(100) in an Ionic Liquid, 1-butyl-3-methyl-imidazolium hexafluorophasphate. *Electrochim. Commun.* **2011**, *13*, 284–286.

(98) Siinor, L.; Arendi, R.; Lust, K.; Lust, E. Influence of Temperature on the Electrochemical Characteristics of Bi(111)|Ionic Liquid Interface. *J. Electroanal. Chem.* **2013**, *689*, 51–56.

(99) See supporting information for additional details of the ion density profiles and structure at the surface.

(100) Lynden-Bell, R. M.; Rasaiah, J. C. From Hydrophobic to Hydrophilic Behaviour: a Simulation Study of Solvation Entropy and Free Energy of Simple Solutes. *J. Chem. Phys.* **1997**, *107*, 1981–1991.

Table 1: Number of cation/anion pairs (N_{IL}), Li^+/anion pairs (N_{Li}), and ranges of total simulation time (t_{sim}) in nanoseconds used for the interface systems.

	[pyr14][TFSI]			[pyr13][FSI]			[EMIM][BF$_4$]		
x_{Li}	N_{IL}	N_{Li}	t_{sim}	N_{IL}	N_{Li}	t_{sim}	N_{IL}	N_{Li}	t_{sim}
0.0	113	0	50-65	147	0	45-55	226	0	40-50
0.2	100	25	60-75	134	33	50-60	212	53	40-50

Table 2: Characteristic formation time of the ionic liquid electric double layer (τ^{edl}) in units of picoseconds as a function of voltage and Li-salt doping.

		τ_{edl}		
$\Delta\Psi$	x_{Li}	[pyr14][TFSI]	[pyr13][FSI]	[EMIM][BF$_4$]
2.1	0.0	193	64	33
	0.2	368	135	160
4.2	0.0	318	216	48
	0.2	395	354	164

Table 3: Potential of zero charge ($\langle\Psi\rangle^0$) and bulk potential ($\langle\Psi\rangle^{\mathrm{B}}$) in units of millivolts for the interface systems.

	[pyr14][TFSI]		[pyr13][FSI]		[EMIM][BF_4]	
x_{Li}	$\langle\Psi\rangle^0$	$\langle\Psi\rangle^{\mathrm{B}}$	$\langle\Psi\rangle^0$	$\langle\Psi\rangle^{\mathrm{B}}$	$\langle\Psi\rangle^0$	$\langle\Psi\rangle^{\mathrm{B}}$
0.00	-61	-794	-112	-12	9	-209
0.20	-54	-641	-109	216	7	37

Table 4: Solvation free energies of Li^+ (F^s) into the ionic liquids electrolytes as resolved into repulsive-dispersive ($\Delta F^{\mathrm{Li}^0(g)\to\mathrm{Li}^0(l)}$) and electrostatic ($\Delta F^{\mathrm{Li}^0(l)\to\mathrm{Li}^+(l)}$) contributions. Units are given in kcal/mol.

	[pyr14][TFSI]	[pyr13][FSI]	[EMIM][BF_4]
F^s	-101.6	-100.8	-97.3
$\Delta F^{\mathrm{Li}^0(g)\to\mathrm{Li}^0(l)}$	4.2	4.7	4.6
$\Delta F^{\mathrm{Li}^0(l)\to\mathrm{Li}^+(l)}$	-105.8	-105.5	-101.9

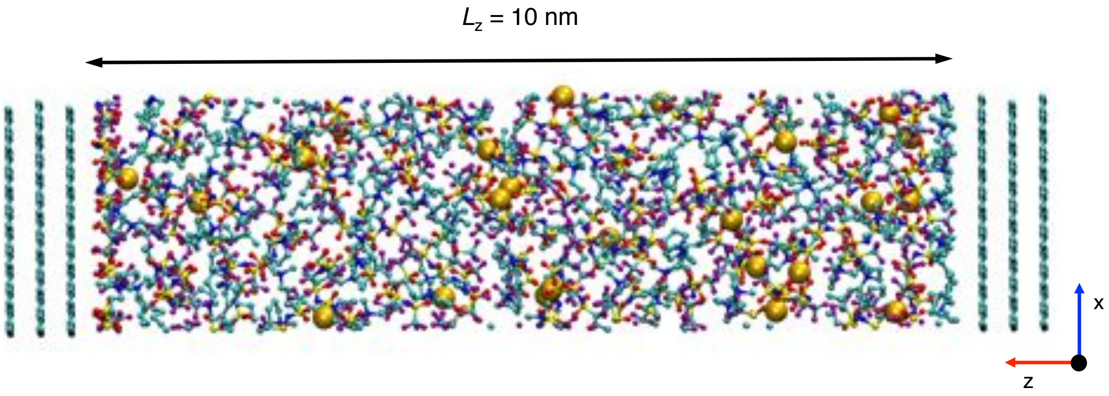

Figure 1: Pictorial example of an ionic liquid (0.8[pyr14][TFSI] + 0.2Li[TFSI]) interfaced with ideal basal-plane graphite electrodes as modeled in the present work. The distance between the electrodes in the non-periodic z-direction, L_z, is 10 nm. Lithium ions are shown as enlarged yellow atoms.

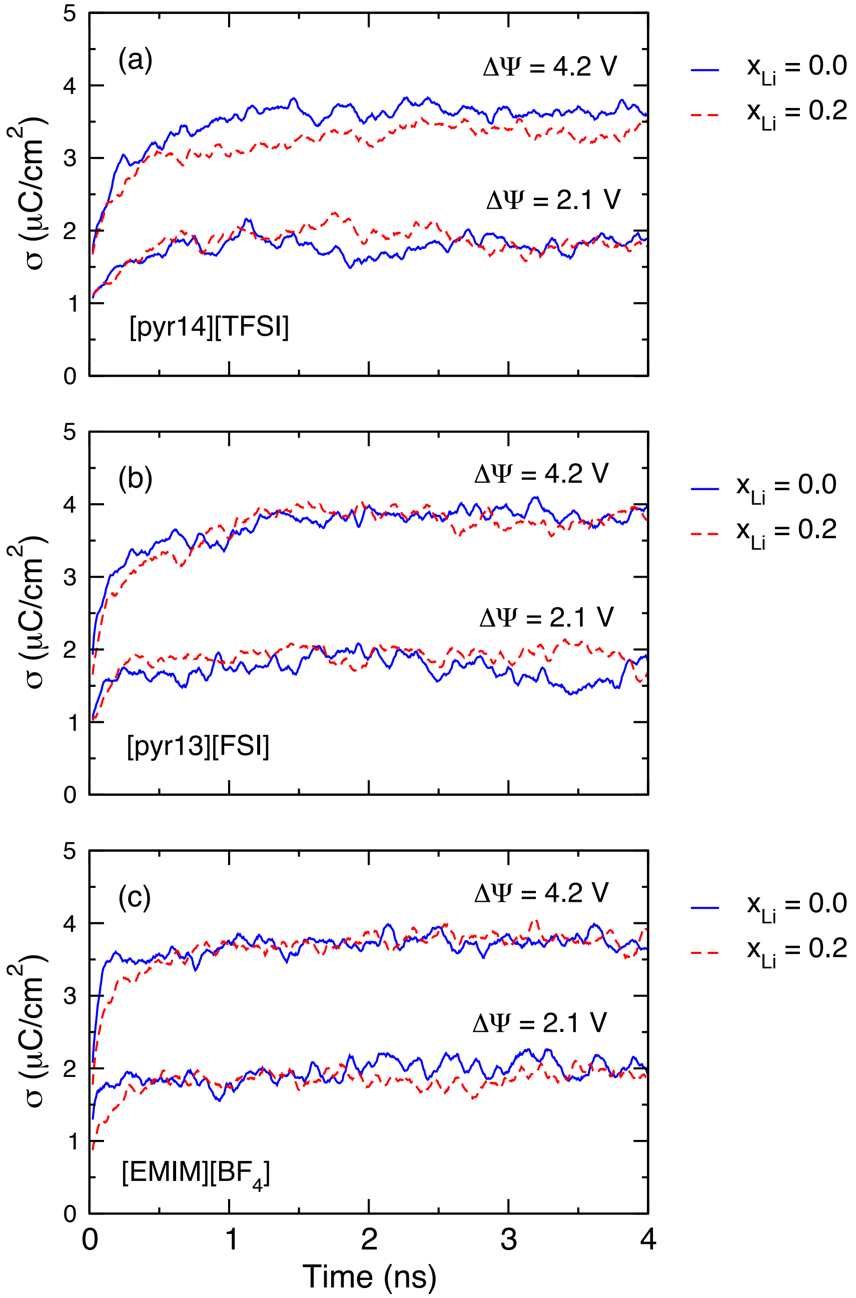

Figure 2: Surface charge density as a function of simulation time for our ionic liquid systems with the $\Delta\Psi$ values of 2.1 and 4.2 V. The initial configurations for these simulations are obtained from the trajectories of $\Delta\Psi = 0$ V simulations.

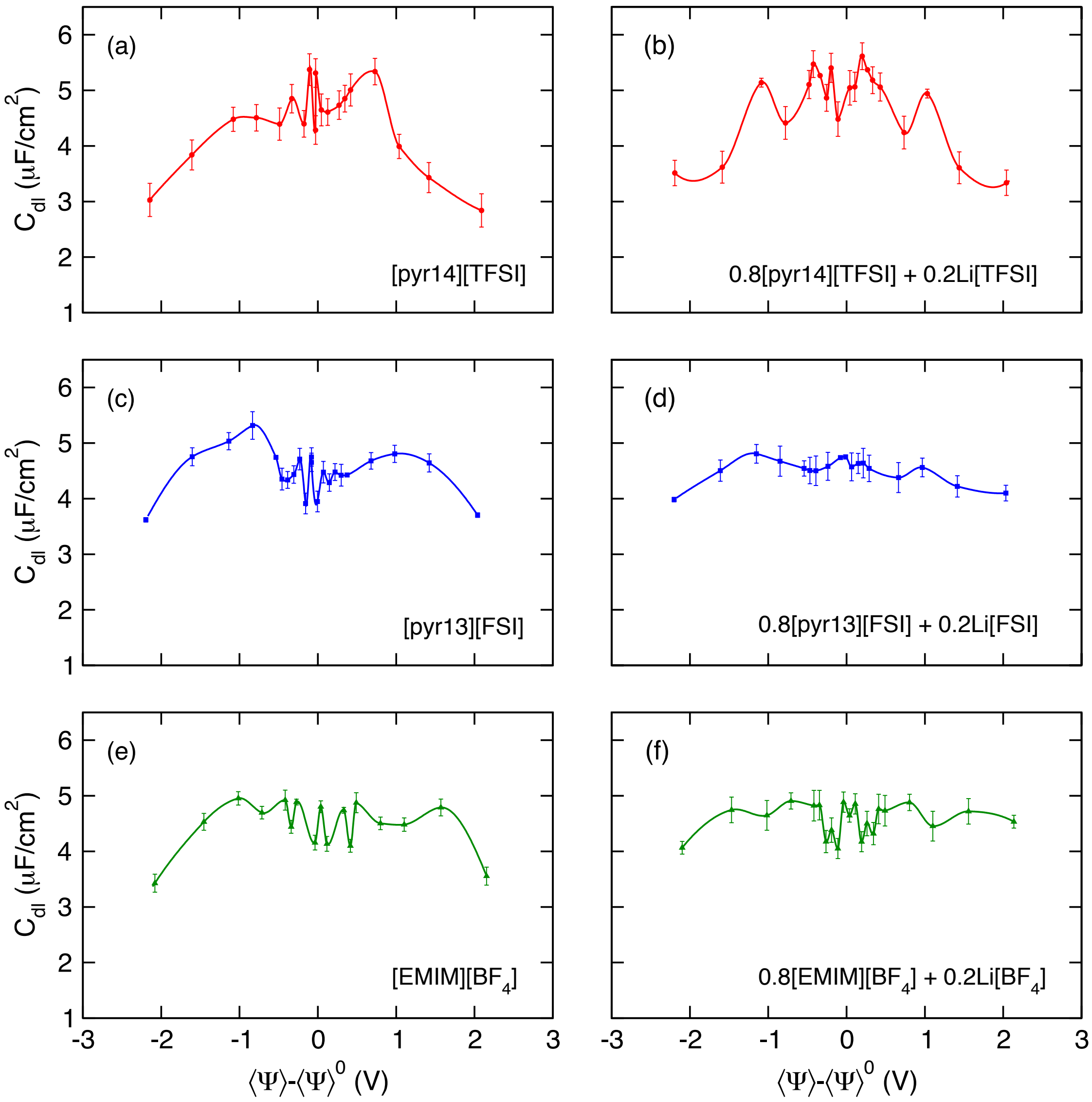

Figure 3: Differential capacitance as a function of surface potential of our three ionic liquid systems having x_{Li} values of 0.0 (a,c,e) and 0.2 (b,d,f). Data in (e) is reproduced from a previous work.[85]

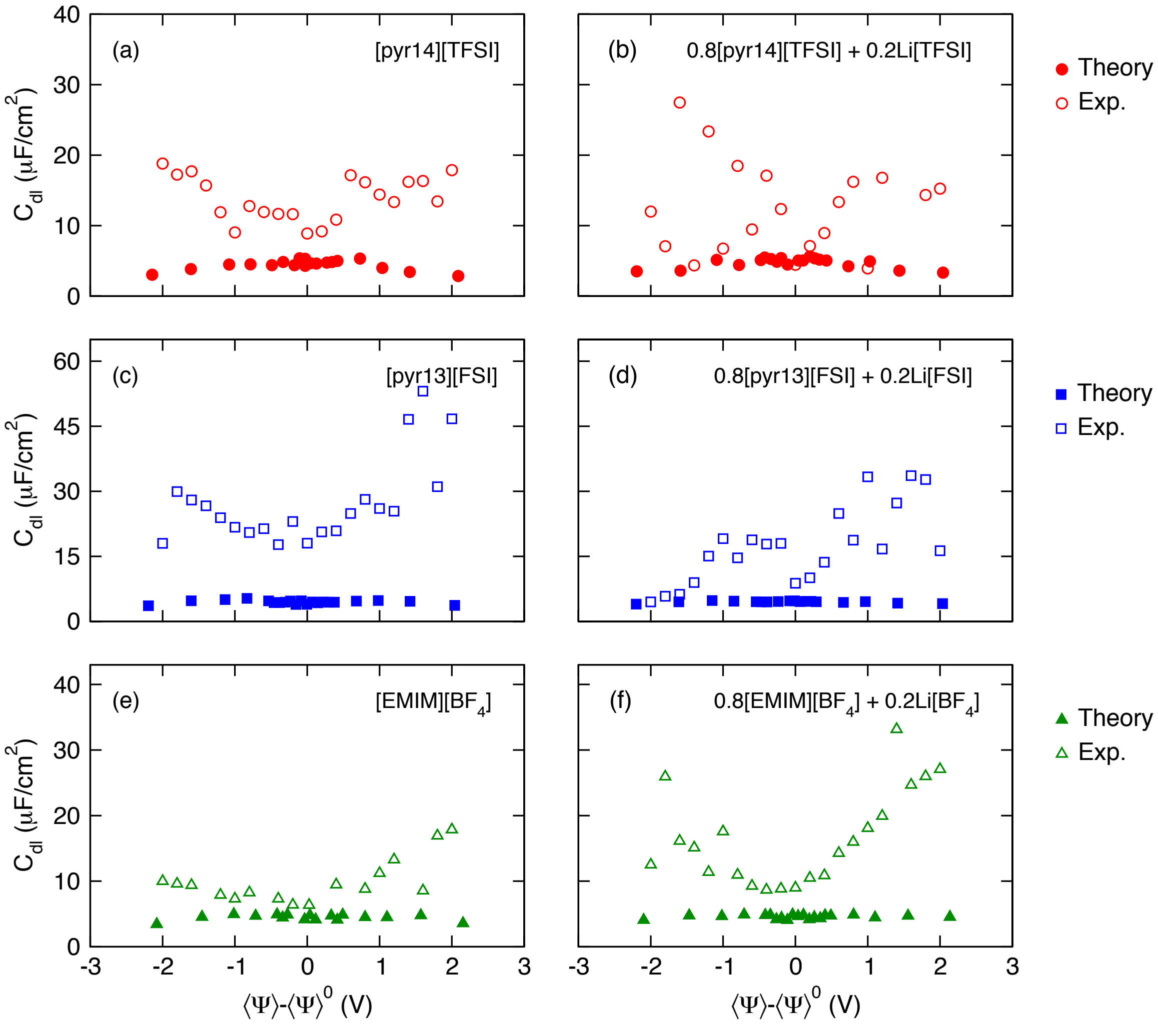

Figure 4: Differential capacitance as a function of surface potential of our three ionic liquid systems having x_{Li} values of 0.0 (a,c,e) and 0.2 (b,d,f). Computational results are shown as solid symbols, while the experimental capacitance on glassy carbon electrodes is given by open symbols.

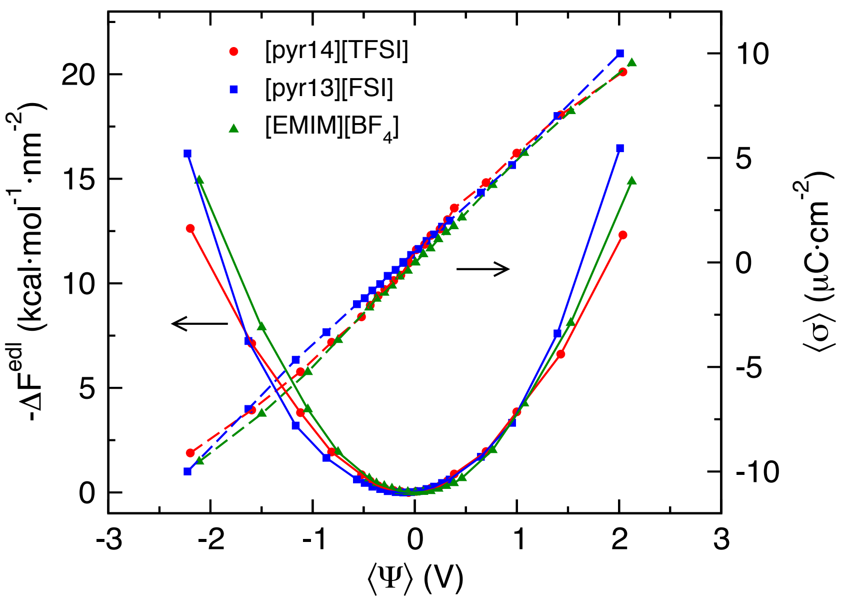

Figure 5: Free energy of EDL formation ($\Delta \mathrm{F}^{\mathrm{edl}}$) (solid lines) and surface charge ($\langle \sigma \rangle$) (dashed lines) as a function of surface potential ($\langle \Psi \rangle$) for the three neat ionic liquids of interest at 363 K. Values of surface charge are included to allow conversion of ΔF^{edl} from a function of $\langle \Psi \rangle$ to $\langle \sigma \rangle$.

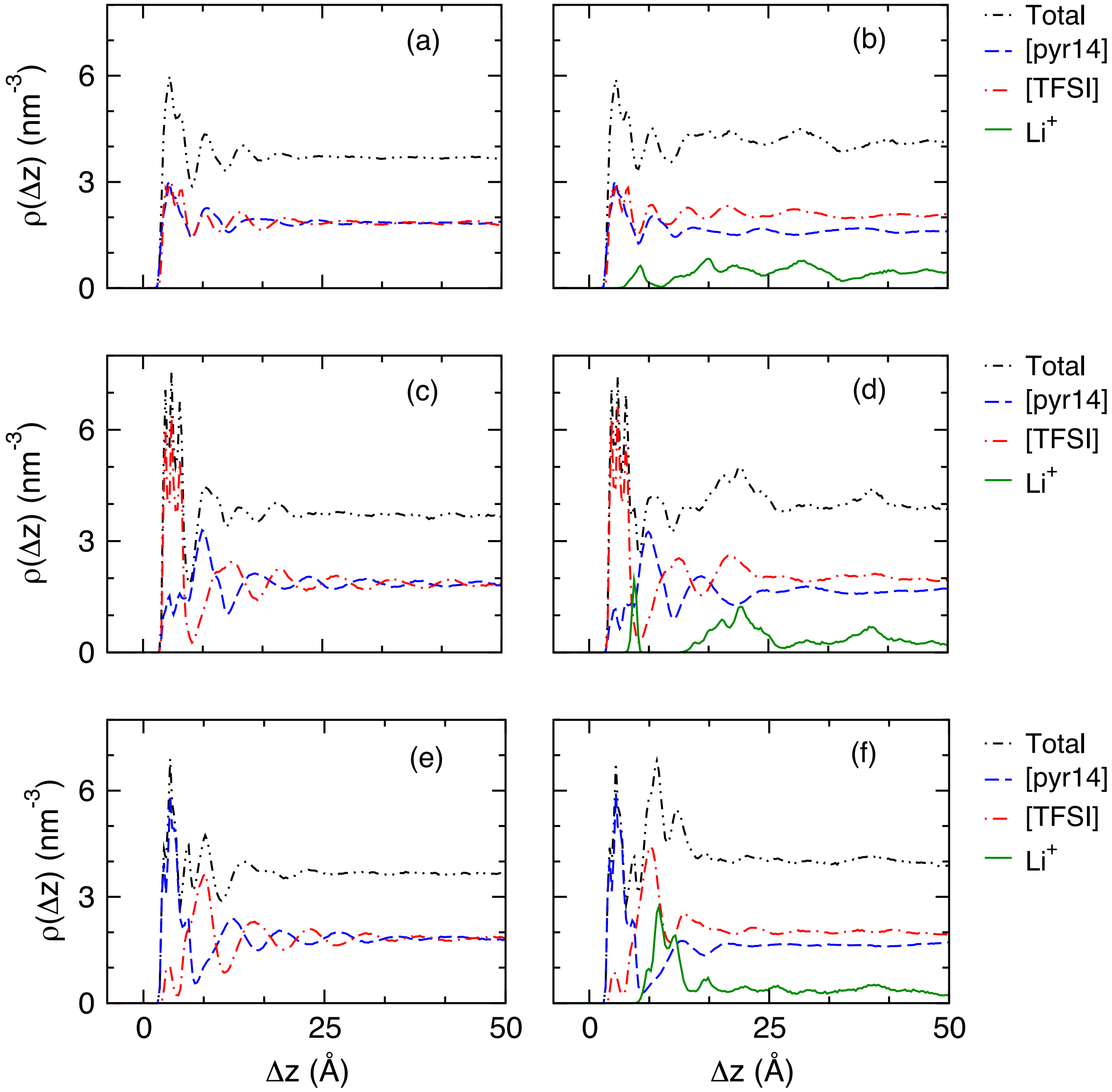

Figure 6: Average density profiles for ions in [pyr14][TFSI] as a function of distance from the (a,b) neutral electrode surface at $\Delta\Psi = 0$ V, (c,d) the cathode surface at $\Delta\Psi = 4.2$ V, and the anode surface at $\Delta\Psi = 4.2$ V. Profiles for both neat [pyr14][TFSI] (a,c,e) as well as that having $x_{\mathrm{Li}} = 0.2$ (b,d,f) are displayed. Data in (e) is reproduced from a previous work.[85]

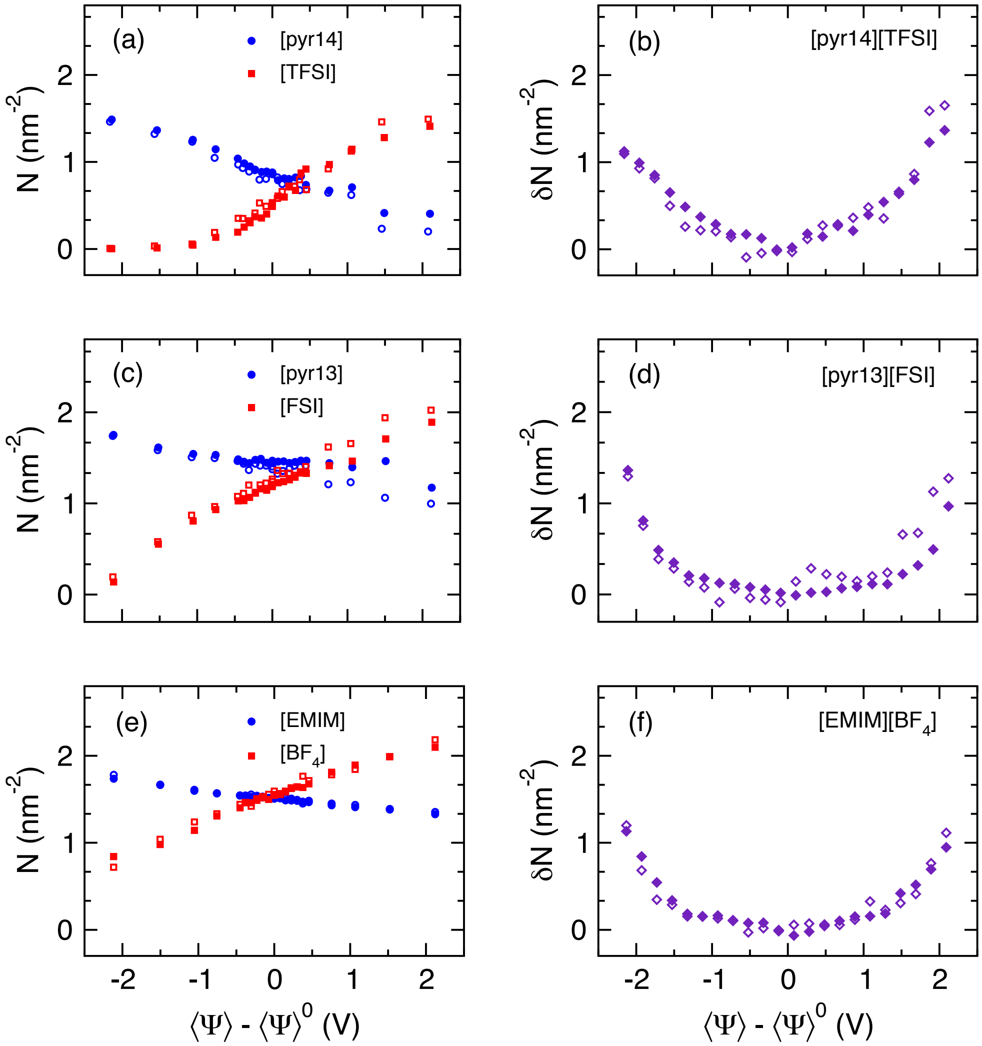

Figure 7: Composition of the surface ion layer, N, (a, c, and e) and net increase in surface ion density, δN (b, d, and f) for ionic liquids having x_{Li} values of 0.0 and 0.2. Potential is referenced to the potential of zero charge found at $\Delta\Psi = 0$ V. Data in (e) is reproduced from a previous work.[85]

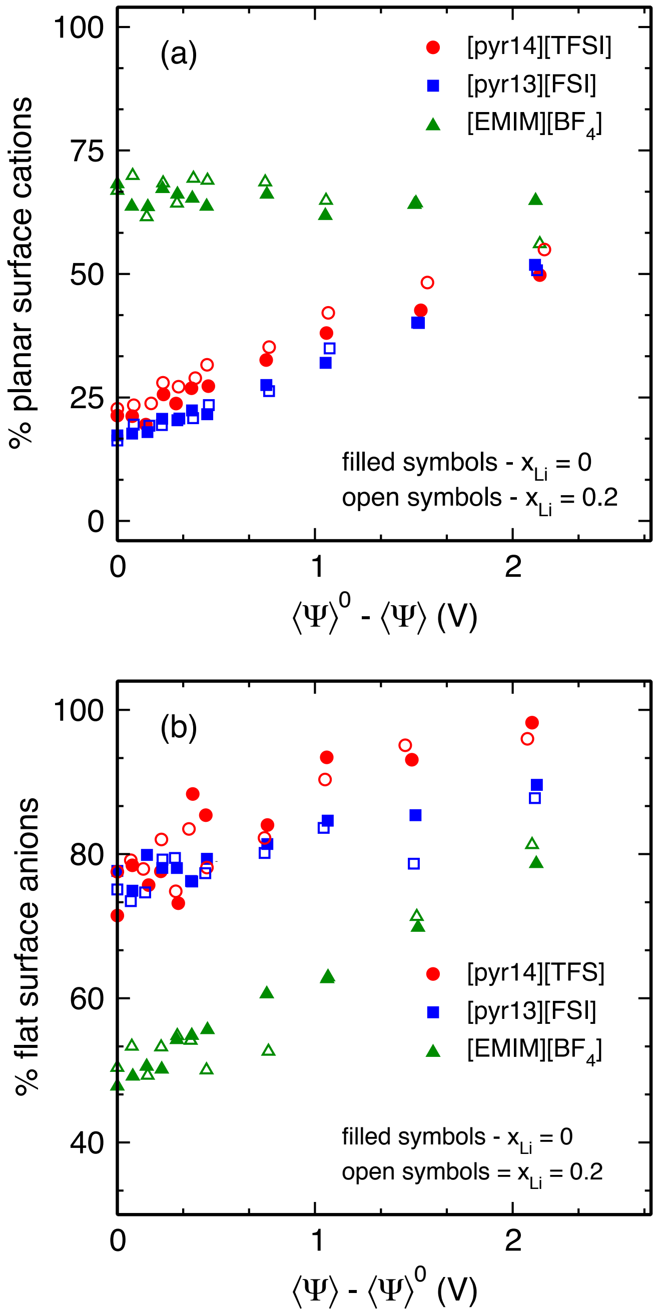

Figure 8: Percent of cations at the electrode surface that are planar (a) and the percent of anions at the electrode surface that lie flat as a function of electrode potential, with potential being referenced to the potential of zero charge found at $\Delta\Psi = 0$ V. Data plotted with filled symbols and open symbols are obtained from systems having x_{Li} values of 0.0 and 0.2, respectively. Data for neat [EMIM][BF$_4$] is reproduced from a previous work.[85]

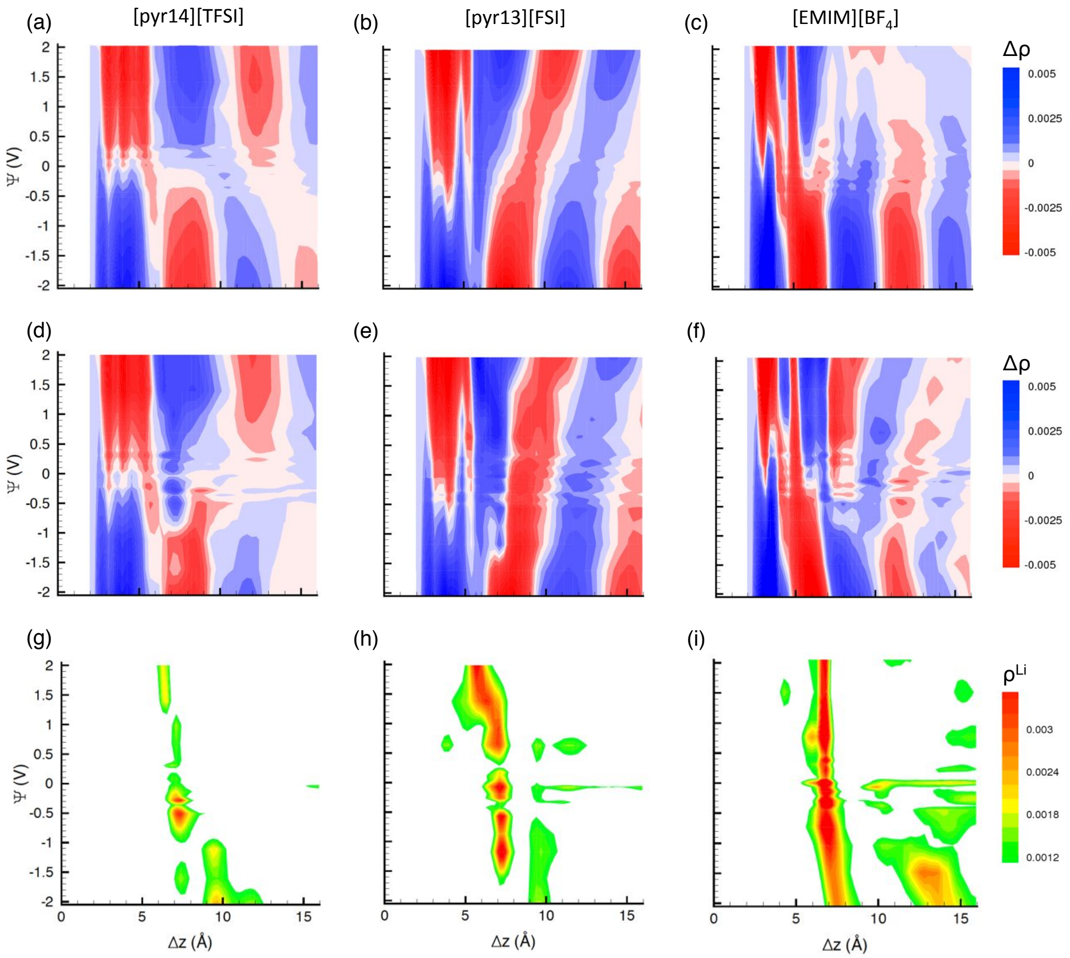

Figure 9: Color contour plot of ion densities in (a,d,g) [pyr14][TFSI], (b,e,h) [pyr13][FSI], and (c,f,i) [EMIM][BF$_4$] as a function of distance from the electrode with 0 V $<\Delta\Psi<$ 4.2 V. Net ion density, or cation density minus anion density, is shown for ionic liquids in the neat form (a,b,c), as well as those having $x_{\mathrm{Li}} = 0.2$ (d,e,f). Also shown is the density of Li^{+} (g,h,i) in ionic liquid systems having $x_{\mathrm{Li}} = 0.2$.

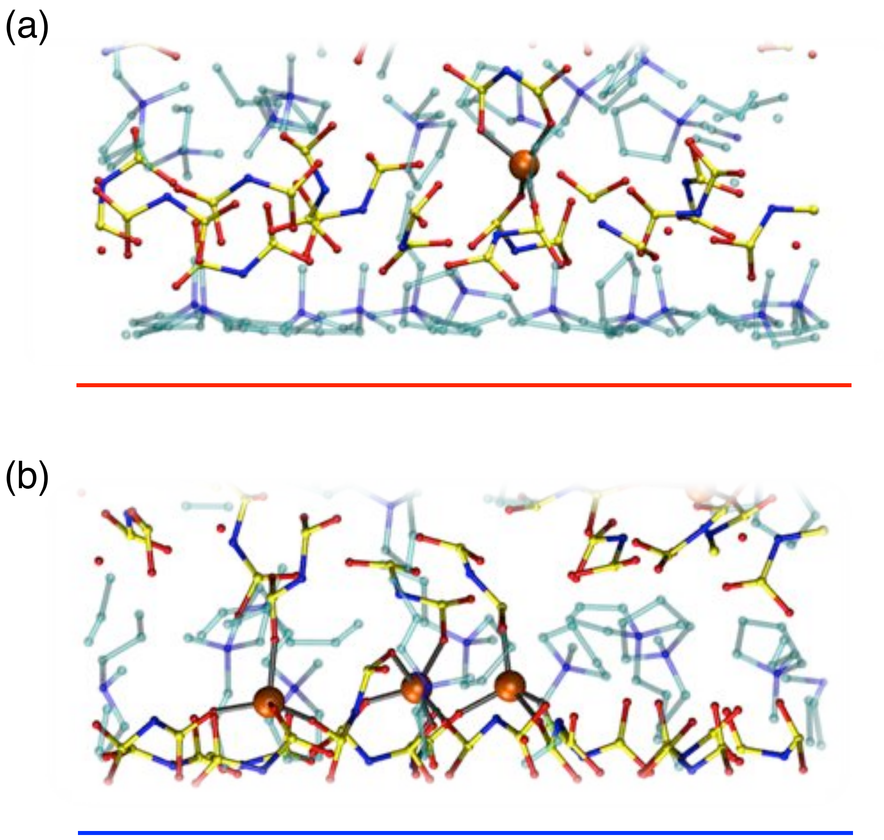

Figure 10: Representative binding of Li^{+} with anions in the double layer at (a) negative electrode potential and (b) positive electrode potential. The red and blue bars indicate the (x,y) plane of the anode and cathode surfaces, respectively.

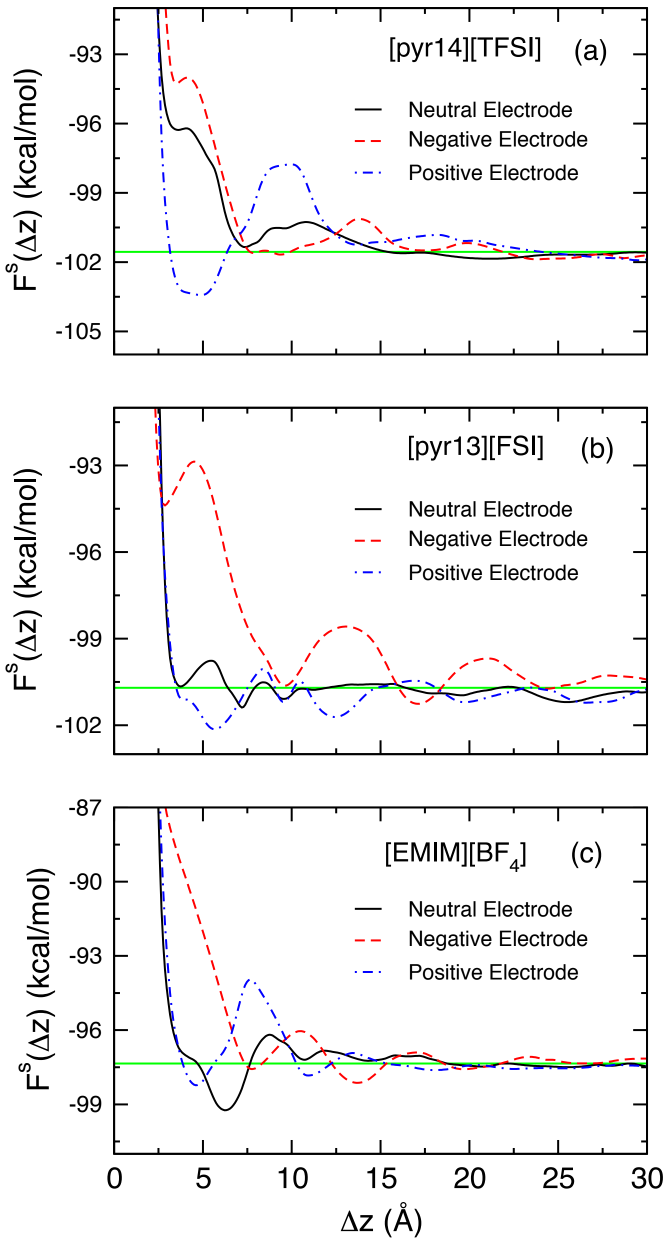

Figure 11: Solvation free energy of Li^+ in our three neat ionic liquids as a function of distance from the electrode. Shown are the F^s profiles against electrodes having $\Delta\Psi = 0$ V (solid black line) as well as against the negative electrode (dashed red line) and the positive electrode (dashed-dotted blue line), where $\Delta\Psi$ between the electrodes is held at 4.2 V.

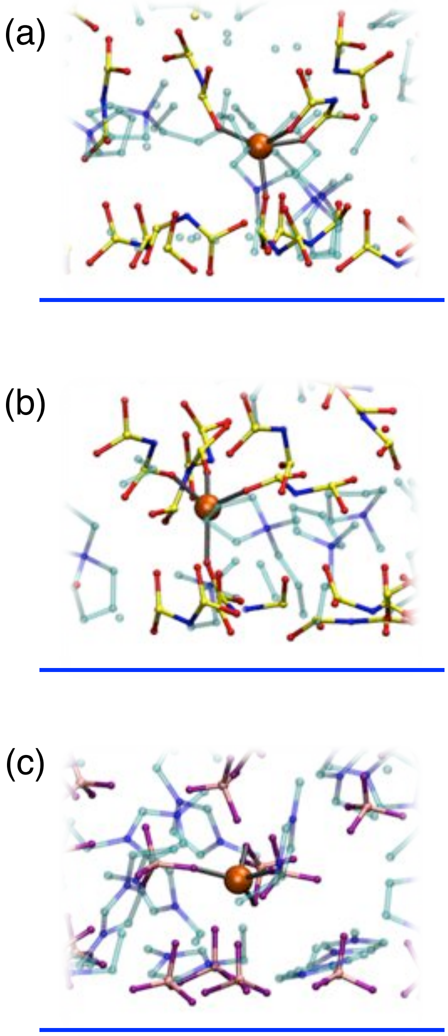

Figure 12: Solvation structure of Li^+ when inserted into the second ion layer adjacent to the positive electrode (cation layer). Structures are shown against the positive electrode of a system have a $\Delta\Psi$ of 4.2 V for (a) [pyr14][TFSI], (b) [pyr13][FSI], and (c) [EMIM][BF_4].

SUPPLEMENTARY MATERIAL

Contents

1. Ion Density Profiles 1
2. Electrostatic Potential Profile 4
3. Ion Center of Mass Profiles 4
4. Ion Surface Configuration 8

1. Ion Density Profiles

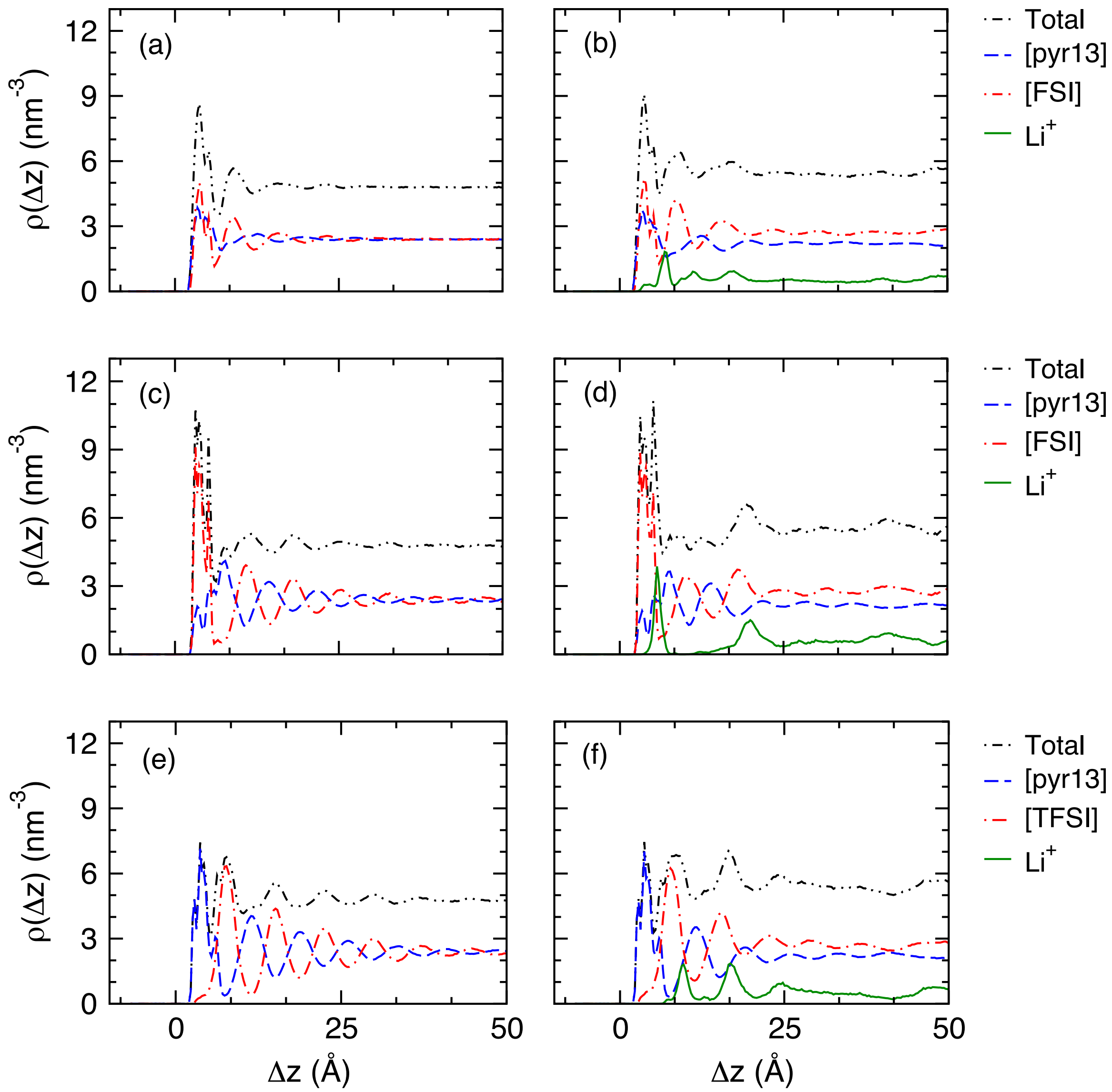

Figure S1. Average atomic density profiles for ions in [pyr13][FSI] as a function of distance from the (a,b) neutral electrode surface at $\Delta\Psi = 0$ V, (c,d) the cathode surface at $\Delta\Psi = 4.2$ V, and the anode surface at $\Delta\Psi = 4.2$ V. Profiles for both neat [pyr13][FSI] (a,c,e) as well as that having $x_{\mathrm{Li}} = 0.2$ (b,d,f) are displayed.

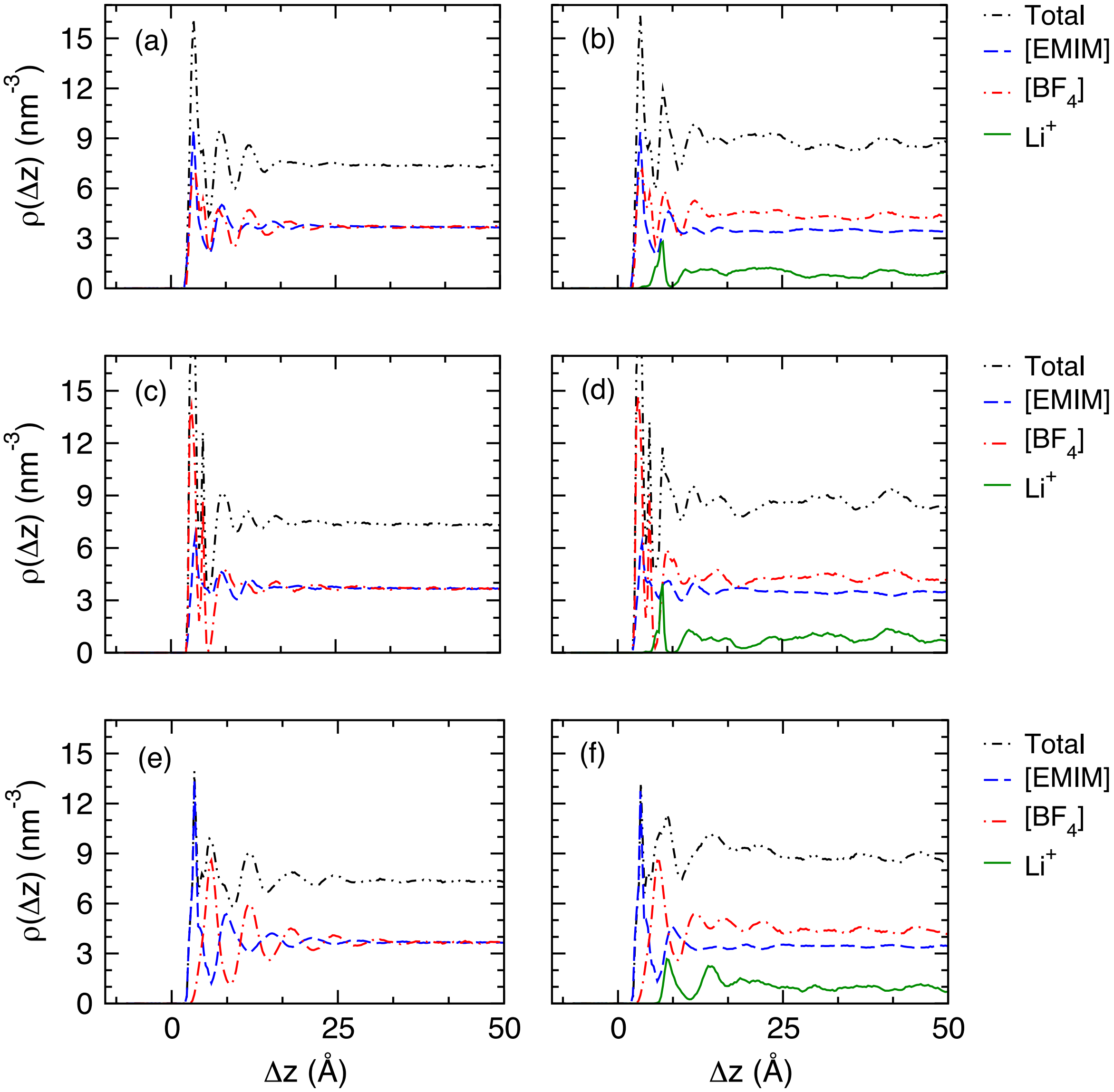

FIGURE S2. Average atomic density profiles for ions in [EMIM][BF$_4$] as a function of distance from the (a,b) neutral electrode surface at $\Delta\Psi = 0$ V, (c,d) the cathode surface at $\Delta\Psi = 4.2$ V, and the anode surface at $\Delta\Psi = 4.2$ V. Profiles for both neat [EMIM][BF$_4$] (a,c,e) as well as that having $x_{\mathrm{Li}} = 0.2$ (b,d,f) are displayed.

2. Electrostatic Potential Profile

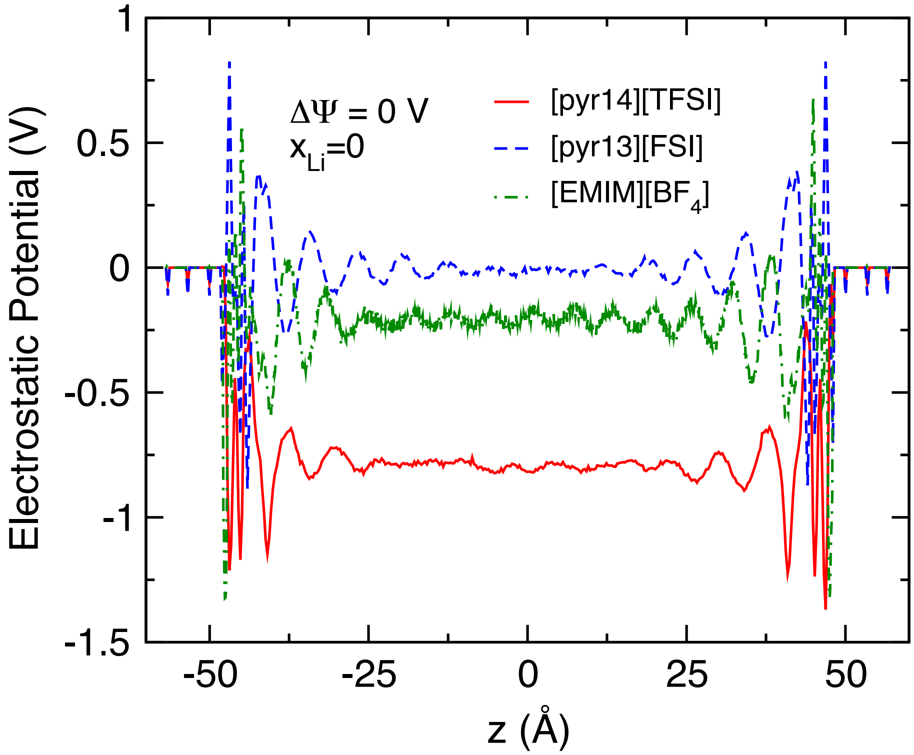

Figure S3. Electrostatic potential as a function of z for our model capacitor system having neat electrolyte and a $\Delta\Psi$ of 0 V.

3. Ion Center of Mass Profiles

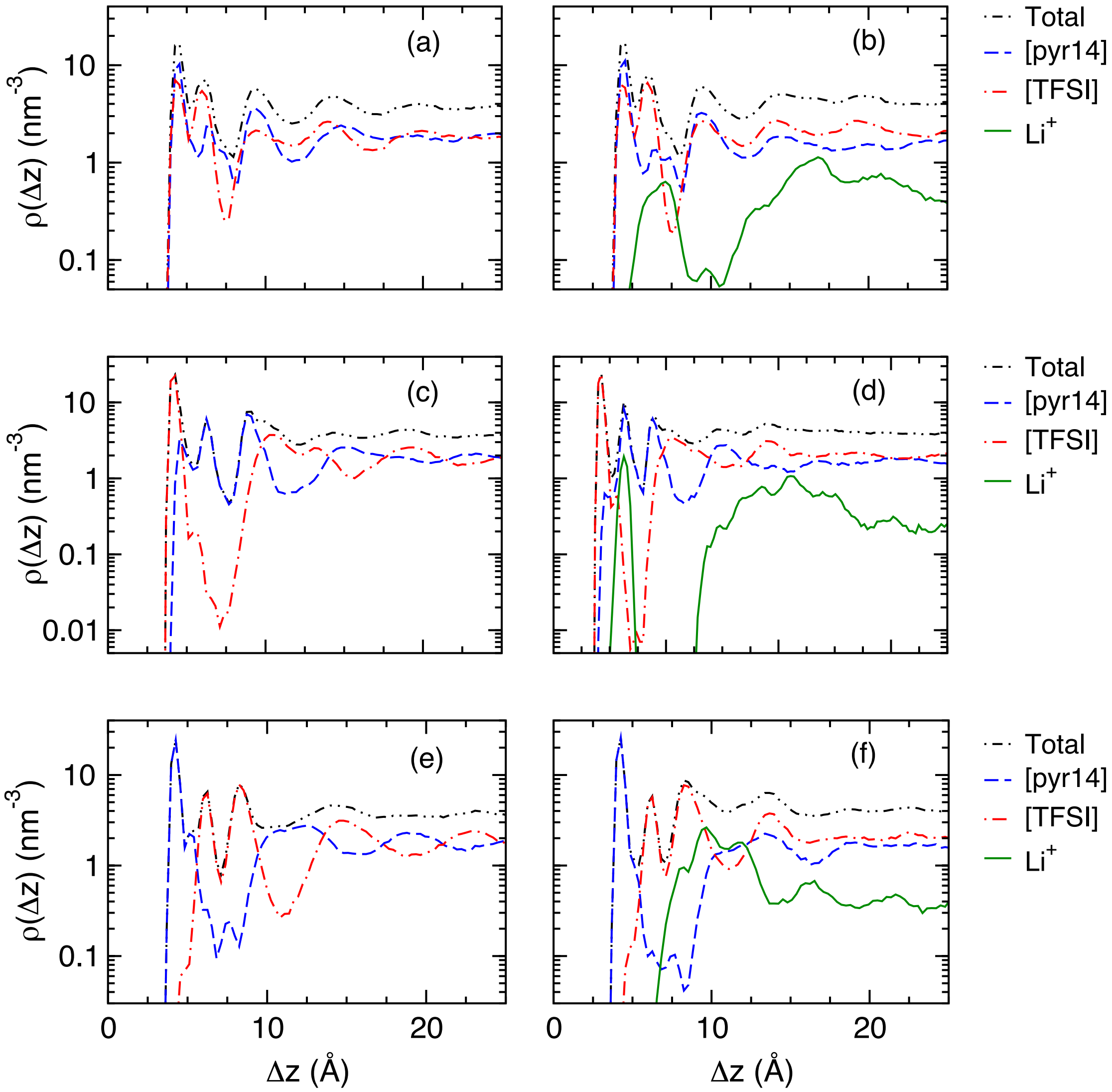

FIGURE S4. Average density profiles of ion centers of mass in [pyr14][TFSI] as a function of distance from the (a,b) neutral electrode surface at $\Delta\Psi = 0$ V, (c,d) the cathode surface at $\Delta\Psi = 4.2$ V, and the anode surface at $\Delta\Psi = 4.2$ V. Profiles for both neat [EMIM][BF$_4$] (a,c,e) as well as that having $x_{\mathrm{Li}} = 0.2$ (b,d,f) are displayed.

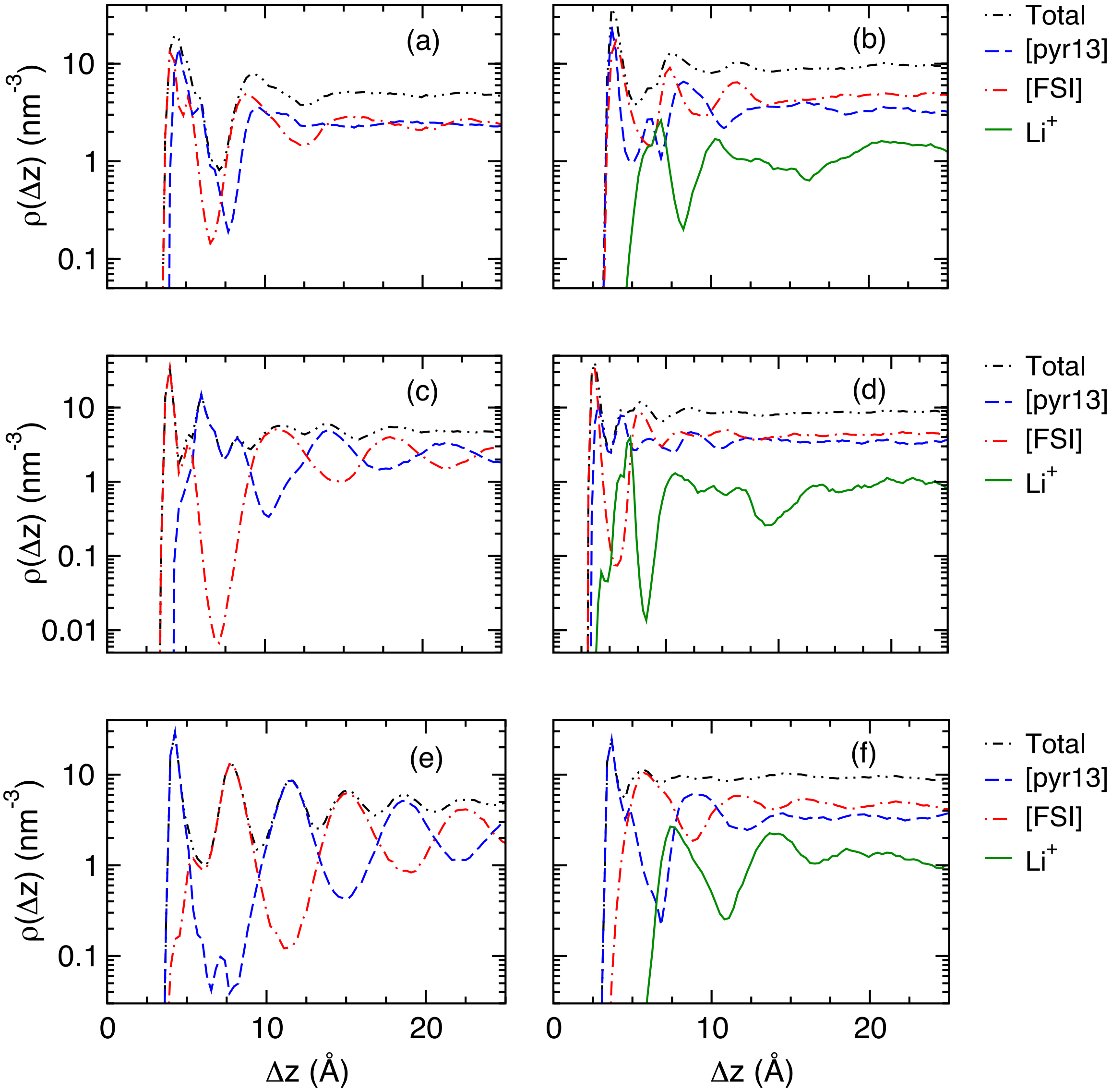

Figure S5. Average density profiles of ion centers of mass in [pyr13][FSI] as a function of distance from the (a,b) neutral electrode surface at $\Delta\Psi = 0$ V, (c,d) the cathode surface at $\Delta\Psi = 4.2$ V, and the anode surface at $\Delta\Psi = 4.2$ V. Profiles for both neat [pyr13][FSI] (a,c,e) as well as that having $x_{\text{Li}} = 0.2$ (b,d,f) are displayed.

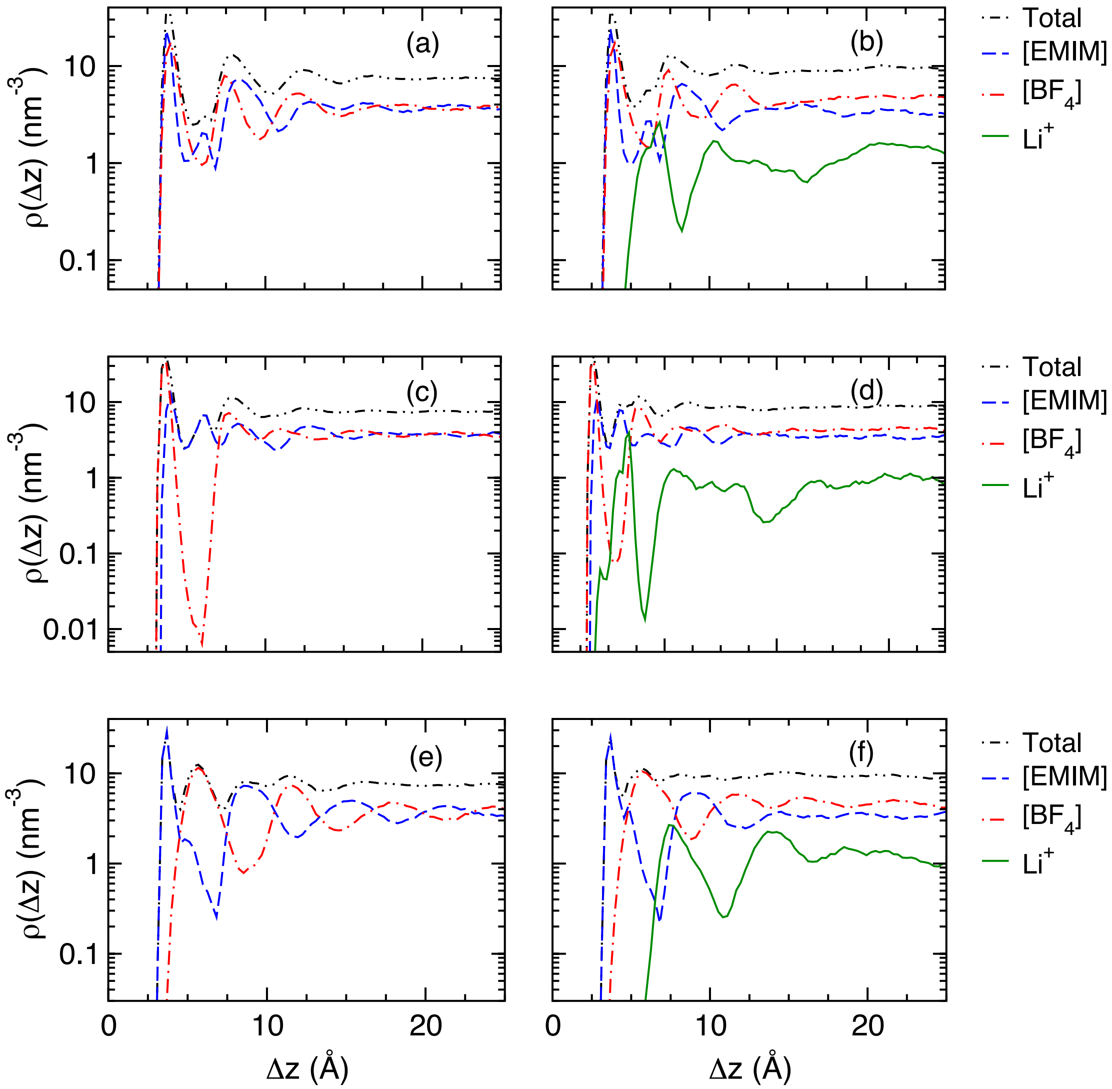

FIGURE S6. Average density profiles of ion centers of mass in [EMIM][BF$_4$] as a function of distance from the (a,b) neutral electrode surface at $\Delta\Psi = 0$ V, (c,d) the cathode surface at $\Delta\Psi = 4.2$ V, and the anode surface at $\Delta\Psi = 4.2$ V. Profiles for both neat [EMIM][BF$_4$] (a,c,e) as well as that having $x_{\mathrm{Li}} = 0.2$ (b,d,f) are displayed.

4. Ion Surface Configuration

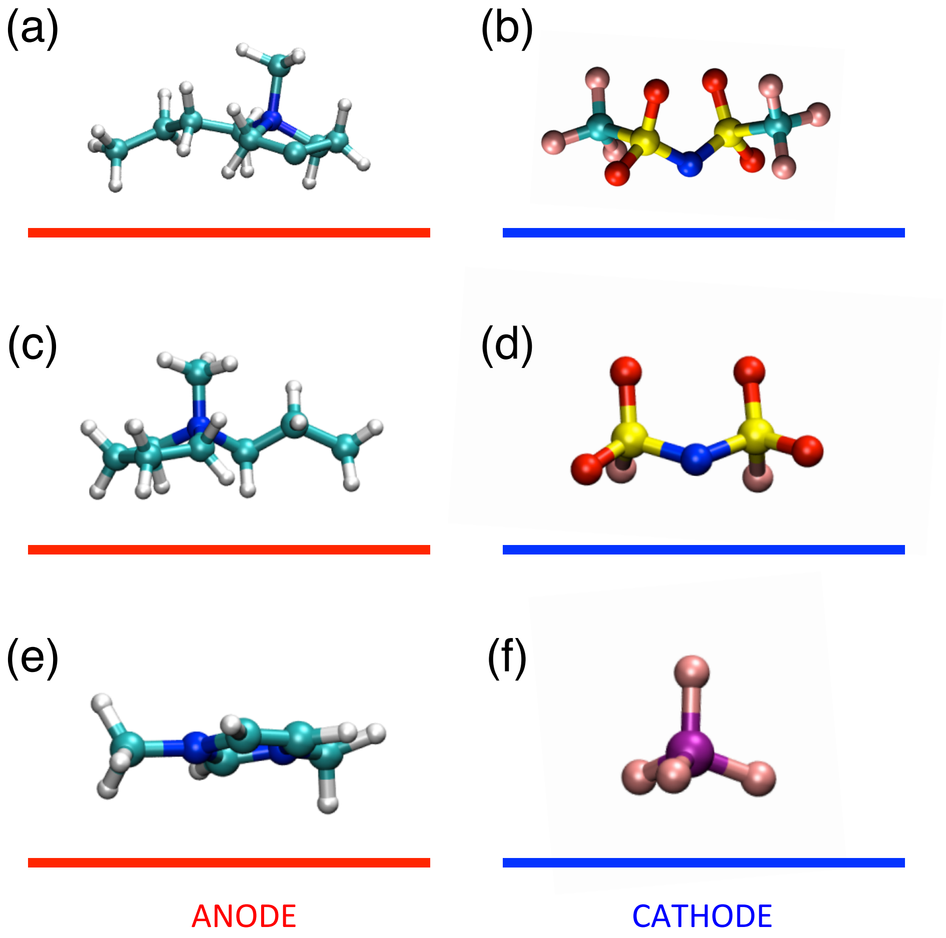

Figure S7. The most common configuration of ionic liquid cations (a,c,e) and anions (b,d,f) at an anode and cathode, respectively, having a $\Delta\Psi$ of 4.2 V. The red and blue bars indicate the (x,y) plane of the anode and cathode surfaces, respectively.

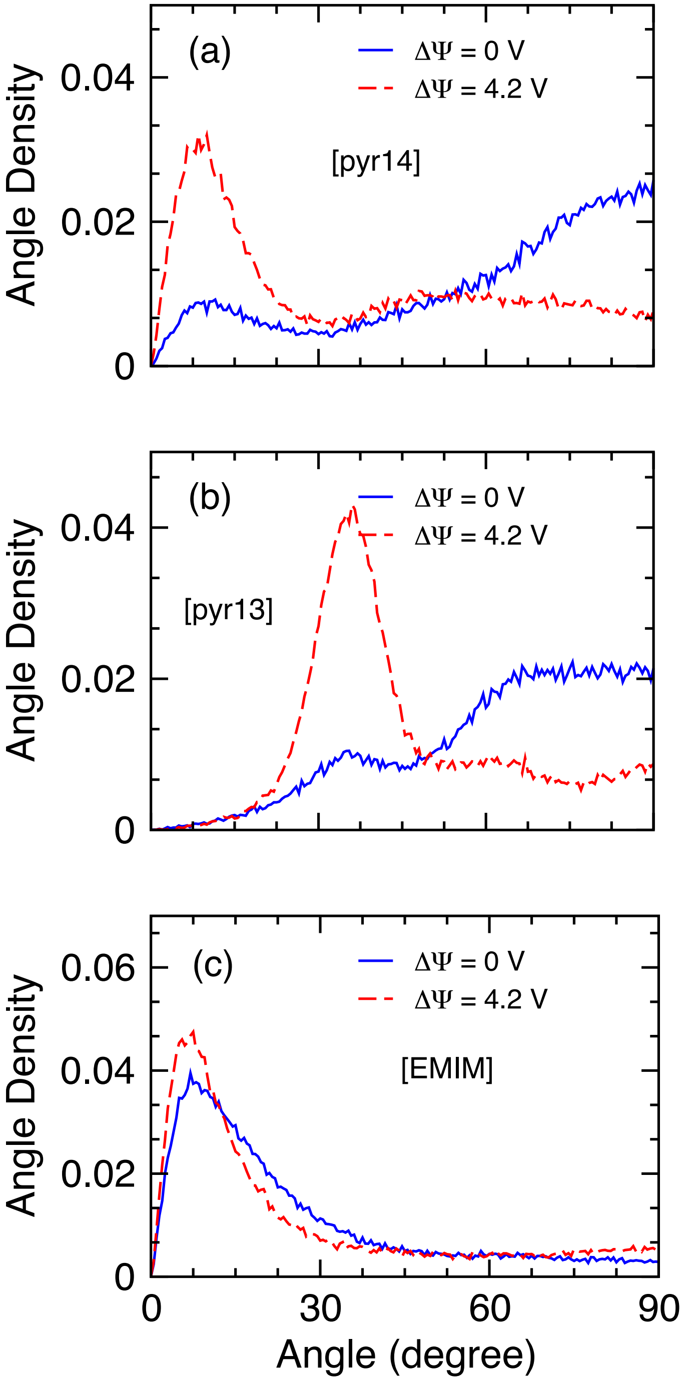

FIGURE S8. Distribution of configuration angles for cations in the surface ion layer from neat ionic liquids at $\Delta\Psi = 0$ and 4.2 V. Given are (a) [pyr14], (b) [pyr13], and (c) [EMIM].

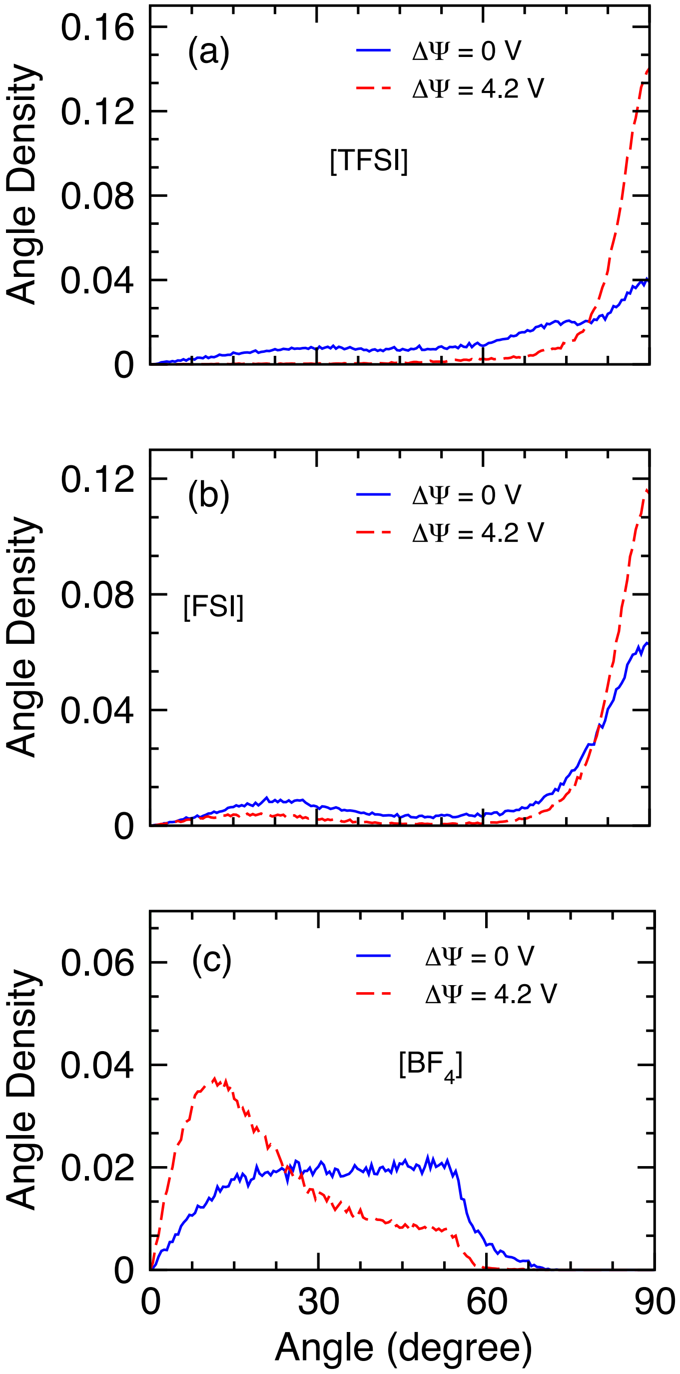

FIGURE S9. Distribution of configuration angles for anions in the surface ion layer from neat ionic liquids at $\Delta\Psi = 0$ and 4.2 V. Given are (a) [TFSI], (b) [FSI], and (c) [BF_4].